Weckmann, U., Magunia, A., Ritter, O. (2005): Effective noise separation for magnetotelluric single site data processing using a frequency domain selection scheme. - *Geophysical Journal International*, *161*, 3, pp. 635—652.

DOI: http://doi.org/10.1111/j.1365-246X.2005.02621.x

Geophys. J. Int. (2005) **161,** 635–652 doi: 10.1111/j.1365-246X.2005.02621.x

Effective noise separation for magnetotelluric single site data processing using a frequency domain selection scheme

U. Weckmann,[1] A. Magunia[2] and O. Ritter[3]

[1] *Dublin Institute for Advanced Studies, School of Cosmic Physics, 5 Merrion Square, Dublin* 2, *Ireland. E-mail: ute@cp.dias.ie*
[2] *Institut für Meteorologie und Geophysik, Universität Frankfurt, Feldbergstr. 45,* D-60323 *Frankfurt, Germany*
[3] *GeoForschungsZentrum, Telegrafenberg,* D-14473 *Potsdam, Germany*

Accepted 2005 February 28. Received 2005 February 28; in original form 2004 October 11

SUMMARY

Magnetotelluric (MT) response function estimates can be severely disturbed by the effects of cultural noise. Methods to isolate and remove these disturbances are typically based on time-series editing, robust statistics, remote reference processing, or some combination of the above. Robust remote reference processing can improve the data quality at a local site, but only if synchronous recordings of at least one additional site are available and if electromagnetic noise between these sites is uncorrelated. If these prerequisites are not met, we suggest an alternative approach for noise removal, based on a combination of frequency domain editing with subsequent single site robust processing. The data pre-selection relies on a thorough visual inspection of a variety of statistical parameters such as spectral power densities, coherences, the distribution of response functions and their errors, etc. Extreme outliers and particularly noisy data segments are excluded from further data processing by setting threshold values for individual parameters. Examples from Namibia and Jordan illustrate that this scheme can improve data quality significantly. However, the examples also suggest that it is not possible to establish generally valid rules for selection as they depend strongly on the local noise conditions. High coherence, for example, can indicate a good signal-to-noise ratio or strongly correlated noise. However, we found that strong polarization of the magnetic field channels and the distribution of response function errors are two important parameters for noise detection.

Key words: data processing, magnetotellurics, signal–noise separation, single site.

1 INTRODUCTION

The magnetotelluric (MT) method is based on measuring time variations of orthogonal components of electric and magnetic fields at the surface of the Earth. The MT impedance tensor $\boldsymbol{Z}$, which generally should be a time invariant quantity is the response of the Earth to electromagnetic induction and carries information about the conductivity distribution of the subsurface. In the frequency domain, the electromagnetic fields are assumed to be linearly related by the impedance tensor $\boldsymbol{Z}$ (e.g. Berdichevsky 1960, 1964; Tikhonov & Berdichevsky 1966):

$$\begin{pmatrix} E_x \\ E_y \end{pmatrix} = \begin{pmatrix} Z_{xx} & Z_{xy} \\ Z_{yx} & Z_{yy} \end{pmatrix} \cdot \begin{pmatrix} B_x \\ B_y \end{pmatrix}, \tag{1}$$

with **E** being the electric field in mV km^{-1}, **B** the magnetic field in nT and $Z_{ij}(i, j = x, y)$ the components of the impedance tensor $\boldsymbol{Z}$ in units of m s^{-1}. A similar relation can be postulated for the vertical magnetic field (e.g. Schmucker 1970):

$$B_z = \begin{pmatrix} T_x & T_y \end{pmatrix} \cdot \begin{pmatrix} B_x \\ B_y \end{pmatrix}, \tag{2}$$

with T_x and T_y as the geomagnetic transfer functions. More generally, the relations above can be described by the following expression:

$$X = Z_1 \cdot Y_1 + Z_2 \cdot Y_2. \tag{3}$$

Usually, the output channel X is associated with either E_x, E_y or B_z and the input channels Y_1 and Y_2 with B_x and B_y, respectively (see eqs 1 and 2); Z_1 and Z_2 are response functions of a linear equation system.

In general, the estimation procedure for the components of $\boldsymbol{Z}$ as well as T_x and T_y is based on least-squares (LSQ) methods; the parameter estimate is chosen in order to minimize the misfit between the predicted (right side of eq. 3) and observed output variable (left side of eq. 3) by minimizing the sum of squared residuals. Results in a LSQ sense are unbiased if noise affects only the output channels of the system (E_x, E_y and B_z in eqs 1 and 2) and

statistically optimal and/or unbiased if noise is independent and Gaussian distributed. In practice, however, these assumptions often fail and LSQ estimates of the impedance tensor can be seriously in error (Junge 1996). This problem has long been identified and is typically addressed by two principal procedures: (i) robust statistics and (ii) the remote reference method. Robust algorithms are based on data adaptive weighting schemes, which aim at detecting and rejecting outliers from a majority of well-behaved samples (Egbert & Booker 1986; Chave *et al.* 1987). However, if a noise source is more persistent, it can easily result in a distribution in which the majority of the data are wrong (i.e. they follow the noise source). In a robust sense, however, this is the correct estimate in that this estimate represents the majority of the data.

The remote reference method requires simultaneously recorded electromagnetic fields from at least two sites that are composed only of correlated signal and uncorrelated noise (Goubau *et al.* 1978; Gamble *et al.* 1979). Typically, the two horizontal magnetic fields are chosen as they usually exhibit lower noise levels than the electric fields. For audio-magnetotelluric (AMT) data, however, the electric fields may be cleaner. The most promising results are achieved with a combination of both methods: a robust remote reference processing (Larsen 1989; Oettinger *et al.* 2001; Chave & Thomson 2004). As robust remote reference processing results have generally been found superior to the simple LSQ approach (Jones *et al.* 1989; Larsen *et al.* 1996; Egbert 1997), they are now routinely applied in MT data processing schemes. It is often difficult, however, to identify a suitable reference site as cultural noise signals can be widespread and coherent over large areas. It is also impossible from a standard MT processing perspective to distinguish between coherent noise and the natural electromagnetic fields. If both local and reference sites are affected by the same noise, the remote reference method can give misleading processing results (Pedersen 1982; Ritter *et al.* 1998). Using data from a local station array, Ritter *et al.* (1998) showed that in some frequency bands up to 99 per cent of the measured time-series were contaminated with correlated noise.

Usually the most severe problem with single site processing are biased response function estimates. The bias is introduced because the LSQ approach requires the input channels Y_1 and Y_2 in eq. (3) to be free of noise (Pedersen 1982). Several methods (Fontes *et al.* 1988; Travassos & Beamish 1988; Hattingh 1989; Jones *et al.* 1989; Tzanis & Beamish 1989; Müller 2000; Chave & Thomson 2004, and references therein) have been suggested to address the bias problem for single site processing. One way to determine the possible extent of bias error is to compute the inverse of $\boldsymbol{Z}$, the admittance tensor. The impedance tensor estimate derived from the admittance tensor is upward biased for any correlated noise in the electric fields. Together with the downward-biased impedance tensor estimates for uncorrelated noise in the magnetic fields, an interval can be given between which lie the unbiased response function estimates (Jones 1980).

Data pre-selection schemes on the basis of coherence or spectral power thresholds have been suggested before (e.g. Jones & Jödicke 1984; Travassos & Beamish 1988; Egbert & Livelybrooks 1996; Smirnov 2003), in practice often with mixed results. However, variable data improvement is not unexpected as this study clearly shows that none of the parameters can be applied in a truly automatic fashion. The method proposed in this paper is a pre-selection scheme that is based on a variety of physical and statistical parameters. However, a thorough visual inspection of the distribution of these parameters is crucial in order to adjust any pre-selection criterion to a particular data set with its specific noise characteristics.

2 DATA SELECTION IN THE FREQUENCY DOMAIN

2.1 Calculation of statistical MT parameters

All of the MT data presented in this paper were gathered using the broad-band instruments from the Geophysical Instrument Pool Potsdam. Typically, five-component electromagnetic field data (b_x, b_y, b_z and e_x, e_y) were recorded as time-series in the frequency range between 2 kHz and 2 mHz. For the data processing, the time-series are bandpass filtered into narrow bands and subsequently divided into short, adjacent segments of fixed length (typically 128 samples). These short segments are cosine tapered prior to the Fourier transformation. In the following, we refer to these (Fourier-transformed) segments as events. The Fourier coefficients are corrected for the influence of the instrument response functions and subsequently they are divided into sub-bands centred around frequencies that are equally distributed on a logarithmic scale. For each of these sub-bands and electromagnetic field components, smoothed autospectra and cross-spectra are computed. The final response function estimates are derived by stacking the single event spectra from all frequency bands using the iterative robust algorithm described in (Ritter *et al.* 1998).

The physical and statistical parameters that we compare in this paper and that we have found useful to assess the data quality are as follows [with $X(\omega)$, $Y_1(\omega)$ and $Y_2(\omega)$ as the parameters described by eq. 3 for one particular frequency].

(i) The spectral power density (e.g. Jenkins & Watts 1968) of input and output channels is defined as

$$\mathrm{pow}(A) = \frac{\sqrt{[AA^*]^2}}{\triangle T}, \tag{4}$$

where $A = X$, Y_1 or Y_2 and $\triangle T$ is the length of the time segment in s. The brackets in eq. (4) denote the smoothed and stacked autospectra with A^* being the complex conjugate of A.

(ii) The bivariate coherences (e.g. Jones 1979) and the partial coherences (e.g. Jenkins & Watts 1968) are, respectively:

$$r^2_{\mathrm{b}} = \frac{Z_1 \cdot [Y_1 X^*] + Z_2 \cdot [Y_2 X^*]}{[XX^*]}; \tag{5}$$

$$r^2_{\mathrm{p}(XY_1)} = \frac{r^2_{\mathrm{b}} - r^2_{\mathrm{u}(XY_2)}}{1 - r^2_{\mathrm{u}(XY_2)}}, \tag{6}$$

$$r^2_{\mathrm{p}(XY_2)} = \frac{r^2_{\mathrm{b}} - r^2_{\mathrm{u}(XY_1)}}{1 - r^2_{\mathrm{u}(XY_1)}}, \tag{7}$$

where the univariate coherence $r^2_{\mathrm{u}(XY)} = \frac{|[XY^*]|^2}{[XX^*][YY^*]}$. The bivariate coherence is the ratio of predicted to measured signal energy between output and input channels under the assumption of a linear relationship between them. In contrast to a natural electromagnetic signal, noisy data often do not fulfill this relationship. One reason might be that the MT sites are often located in the near field of the noise sources and thus the plane wave assumption as well as the orthogonality and the proportionality of the electric and magnetic field are violated (Boerner *et al.* 1993). As the latter results in lower bivariate coherence values, this parameter is commonly regarded as an indicator of data quality. As the coherences are normalized quantities, their values lie in the range (0,1).

(iii) The polarization directions α_E and α_B of the electric and magnetic wave field (Fowler *et al.* 1967) are, respectively,

$$\alpha_E = \arctan \frac{2 \cdot Re([ExEy^*])}{[ExEx^*] - [EyEy^*]} \tag{8}$$

and

$$\alpha_B = \arctan \frac{2 \cdot Re([BxBy^*])}{[BxBx^*] - [ByBy^*]}, \tag{9}$$

and describe the time-harmonic variation of two orthogonal field components with constant phasing. Natural magnetic signal is generated by a variety of sources, such as solar activity, ionospheric current systems and lightning. These sources generate magnetic fields that vary in their incidence directions and thus we do not expect a preferred polarization direction for the magnetic field. However, according to a given conductivity distribution of the subsurface, there might be a preferred polarization direction of the induced electric field.

(iv) The response functions and their statistical errors are:

$$Z_1 = \frac{[XY_1^*][Y_2Y_2^*] - [Y_2Y_1^*][XY_2^*]}{[Y_1Y_1^*][Y_2Y_2^*] - |[Y_1Y_2^*]|^2}, \tag{10}$$

$$Z_2 = \frac{[Y_1Y_1^*][XY_2^*] - [Y_1Y_2^*][XY_1^*]}{[Y_1Y_1^*][Y_2Y_2^*] - |[Y_1Y_2^*]|^2}, \tag{11}$$

$$|\delta Z_1|^2 = \frac{(1 - r_b^2) \cdot [XX^*][Y_2Y_2^*]}{[Y_1Y_1^*][Y_2Y_2^*] - |[Y_1Y_2^*]|^2} \cdot \frac{4}{\nu - 4} \cdot F_{4,\nu-4,1-\alpha}, \tag{12}$$

$$|\delta Z_2|^2 = \frac{(1 - r_b^2) \cdot [XX^*][Y_1Y_1^*]}{[Y_1Y_1^*][Y_2Y_2^*] - |[Y_1Y_2^*]|^2} \cdot \frac{4}{\nu - 4} \cdot F_{4,\nu-4,1-\alpha}, \tag{13}$$

with ν as the number of degrees of freedom, $F_{4,\nu-4,1-\alpha}$ as the Fisher F distribution with a chosen probability $\alpha = 68$ per cent.

The error calculation used herein estimates the statistical error of the response functions Z_1 and Z_2, which are calculated from the ratio of χ^2-distributed quantities (autospectra and cross-spectra) and thus are regarded as Fisher F distributed random variables (Fisher 1922). However, this error estimation is based on simplifying assumptions, such as the stationarity of signals or the Gaussian distribution of the random variables, for example, leading to biased error bounds. A discussion of the accuracy of the statistical error estimation or a comparison with non-parametric estimators, like the jackknife method (Chave & Thomson 1989) is beyond the scope of this paper.

Although the statistical error estimator might be biased, a comparison between events is still appropriate and meaningful as a criterion for data selection. Besides the Fisher F distribution, the expression for the statistical error (see eqs 12 and 13) contains the autospectra and cross-spectra of all channels and the bivariate quadratic coherence. If the bivariate coherences are high ($\approx$1), we can expect that the response function errors vanish or become very small. However, the statistical error will more likely indicate the presence of noise in the input channels than the bivariate quadratic coherence, because the denominator of the statistical error contains the autospectra of both input channels.

2.2 Variation of statistical parameters and their depiction

When examining the above mentioned statistical parameters, we are mainly interested in their variations over time. As all of these parameters are computed for each event and frequency, the depiction of consecutive events represents a time axis. We can thus derive graphs showing the variations of statistical and physical properties throughout the entire recording interval. Fig. 1 shows how the graphs are displayed in the frequency domain. The title bar includes the frequency and the selected channels for X, Y_1 and Y_2 as well as the site number. The upper panel of graphs displays the spectral power densities of the three channels determining the bivariate system (windows a–c). Because of the rotation of the Earth and varying strength of ionospheric and magnetospheric sources, the natural high-frequency electromagnetic signal, strictly speaking its spectral power density, shows smooth daily variations (Szarka 1988; Garcia & Jones 2002). Contamination with noise often appears to be random in time and shows a variable pattern throughout the day. Windows (d) and (g) show the response functions Z_1 and Z_2 in the complex plane (Argand diagram). The impedance estimates calculated from the ratio of electric and magnetic fields are stationary quantities mainly because of the stationarity of the signal itself and constant length time windows are used to calculate the estimates. However, if noise influences some channels, the resulting response functions are not necessarily stationary. The averaged response function estimate calculated from the entire data set is shown as a cross in windows (d) and (g).

The statistical errors of both response function estimates (Fig. 1e), both partial coherences (i) and electric and magnetic polarization directions (h) are plotted in one graph each. Before plotting the statistical parameters, all events are checked whether their bivariate coherences (f) lie in the range (0,1); events out of these bounds are rejected automatically as they are probably caused by processes that depart from the correct LSQ estimate or by numerical instabilities.

For data selection, upper and lower thresholds for each of the parameters are chosen. Events located outside these bounds are excluded from further processing and are no longer displayed. The averaged response function is recalculated from the arithmetic average values of the remaining cross-spectra and autospectra. If preselection is successful, an approximately circular-shaped cluster of response function estimates in windows (d) and (g) is obtained, which is a necessary but not sufficient condition for a Gaussian distribution (see also Fig. 5). We would expect the cross, indicating the averaged response function, to be located close to the centre of the distribution of the response function estimates. A cross not close to the centre of the cluster indicates strong outliers present in the data, which shift the mean value of the response function estimates.

3 CASE STUDIES

The majority of the field data discussed hereafter were collected in the vicinity of the Dead Sea transform in Jordan. Within the framework of the DEad SEa Rift Transect (DESERT) project (DESERT Research Group 2000; Ritter *et al.* 2003a), electromagnetic data were measured at more than 250 sites between 2000 to 2003 using the SPAM MKIII (Ritter *et al.* 1998) and CASTLE systems of the Geophysical Instrument Pool Potsdam. The typical recording time at each site was three days. Local remote referencing was possible as up to three sites were recorded simultaneously. One of the example responses was recorded at a site in northwest Namibia in 1999 using the same instrumentation (Ritter *et al.* 2003b; Weckmann *et al.* 2003).

The data sets in Jordan and Namibia were gathered mostly in remote desert areas, which generally exhibit very low levels of cultural noise, which ensures high data quality. Some sites, however, showed strongly disturbed data. In Jordan, most of these sites were located near the border with Israel in close proximity to military installations. Further electromagnetic noise sources were irrigation

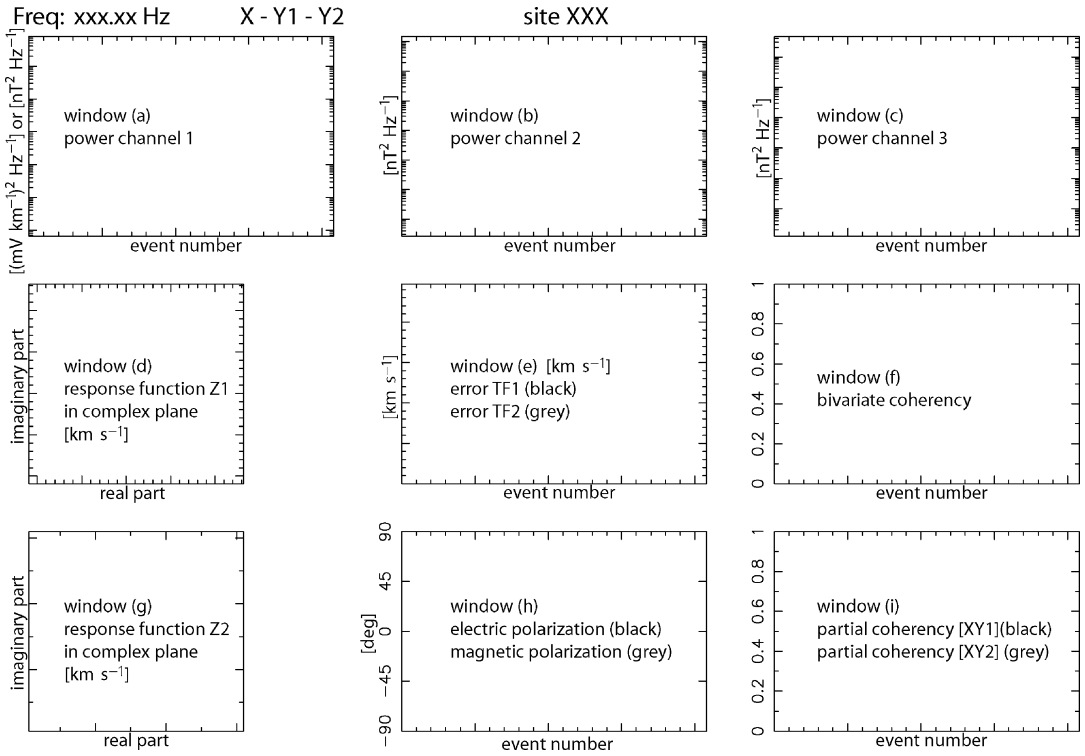

Figure 1. The title bar of the graphical selection program includes the selected frequency, the three channels of a bivariate equation system (see eq. 3) and the site number. The x-axis of most graphs shows the event number, which is a proxy for time and spans the entire recording interval. The two response function plots (d) and (g) are displayed in the complex plane (Argand diagram).

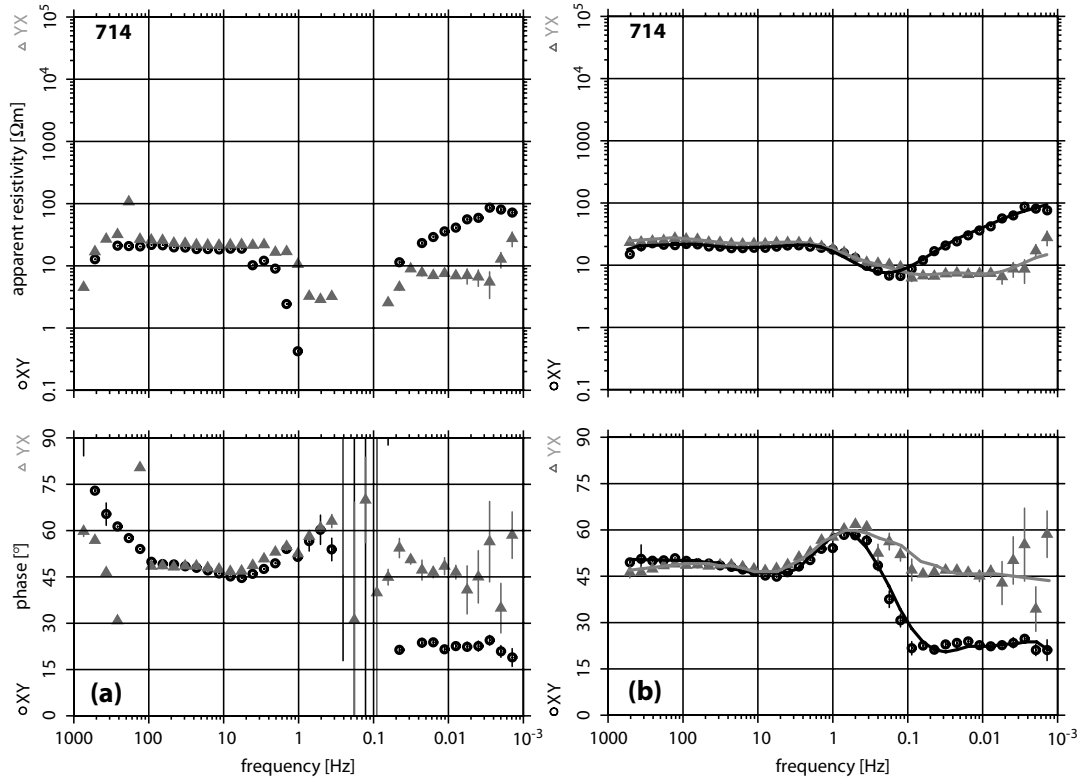

Figure 2. Apparent resistivity and phase curves of site 714 obtained after applying robust processing (a). Both off-diagonal components of the impedance tensor are severely biased between 4 and 0.03 Hz and for frequencies higher than 128 Hz. (b) Applying data pre-selection in combination with robust single site processing improves the results significantly. The solid lines indicate the theoretical apparent resistivity and phase curves obtained from applying the D+ algorithm (Beamish & Travassos 1992).

systems (water pumps) in Israel and mobile phone transmitters along the desert highway in the Arava valley.

In view of the very clean data collected in the desert, we could learn much about the large variety of noise sources at the contaminated sites. In the following, we will show that this noise can be identified and removed effectively from a data set so that even severely disturbed apparent resistivity and phase curves are recovered. The examples given are generally helpful to develop strategies for noise recognition in MT data.

3.1 Simple noise

The first example describes a simple case for data selection, as it is easy to distinguish between undisturbed and noisy data segments. Fig. 2(a) shows the apparent resistivity and phase curves of both off-diagonal components of the impedance tensor at site 714. All curves are severely distorted between 4 and 0.03 Hz and also for frequencies higher than 128 Hz. We investigate the data distribution at an exemplary frequency of 362 Hz. The higher the chosen frequency, the more events are available, which results in a much higher resolution plot than in the case of only a few events.

Fig. 3 shows the statistical parameters described in the previous section using the input channels B_x and B_y, which relate the output channel E_x to the response functions $Z1 = Z_{xx}$ and $Z2 = Z_{xy}$. In the following, characters in brackets refer to the window position in the graphs (see Fig. 1). The spectral power densities of E_x (a) and B_x (b) exhibit the expected distribution of a varying natural signal activity, typically with a spread of approximately two decades. The power distribution of B_y (c), on the other hand, indicates an abrupt increase accompanied by a much smaller spread for all event numbers greater than 3000. At the same event counter, we observe a drop in the bivariate coherence (f) and a change in polarization directions of the magnetic field (h) in terms of a preferred polarization direction of $\pm$ 90. These last $\sim$1200 events also cause the smaller of two clusters of the response function estimates Z_{xy} in window (g). Fig. 4 is derived after rejecting all events with bivariate coherence less than 0.95. The light grey dots in windows (d) and (g) indicate all those events that were omitted for the recalculation and also for a subsequent robust stacking; from a total of 4160 events, only 520 had sufficiently high coherence. Clearly, this selection could remove the smaller cluster in Fig. 3(g) from the data set and the remaining response function estimates appear more focussed (g) when compared with the corresponding plot in Fig. 3 and furthermore form a circular cluster indicating an approximately Gaussian distribution. Fig. 5 shows the distribution of $Re(Z_{yx})$ and $Im(Z_{yx})$ before (see Fig. 3g) and after selection (Fig. 4g). The two peaks visible in Figs 5(a) and (b) represent the two clusters in Fig. 3(g). After selection (Figs 5c and d), the distribution of $Re(Z_{yx})$ and $Im(Z_{yx})$ approximately obeys a Gaussian distribution indicated by the black solid line.

Another commonly applied data selection procedure is to identify and remove all events with phase values outside of the assigned quadrant. This phase criterion is based on the fact that phase values are restricted to a specific quadrant for 1-D and 2-D electrical conductivity structure (Weidelt & Kaikkonen 1994). In the absence of noise, phase values are in the first quadrant for Z_{xy} and in the

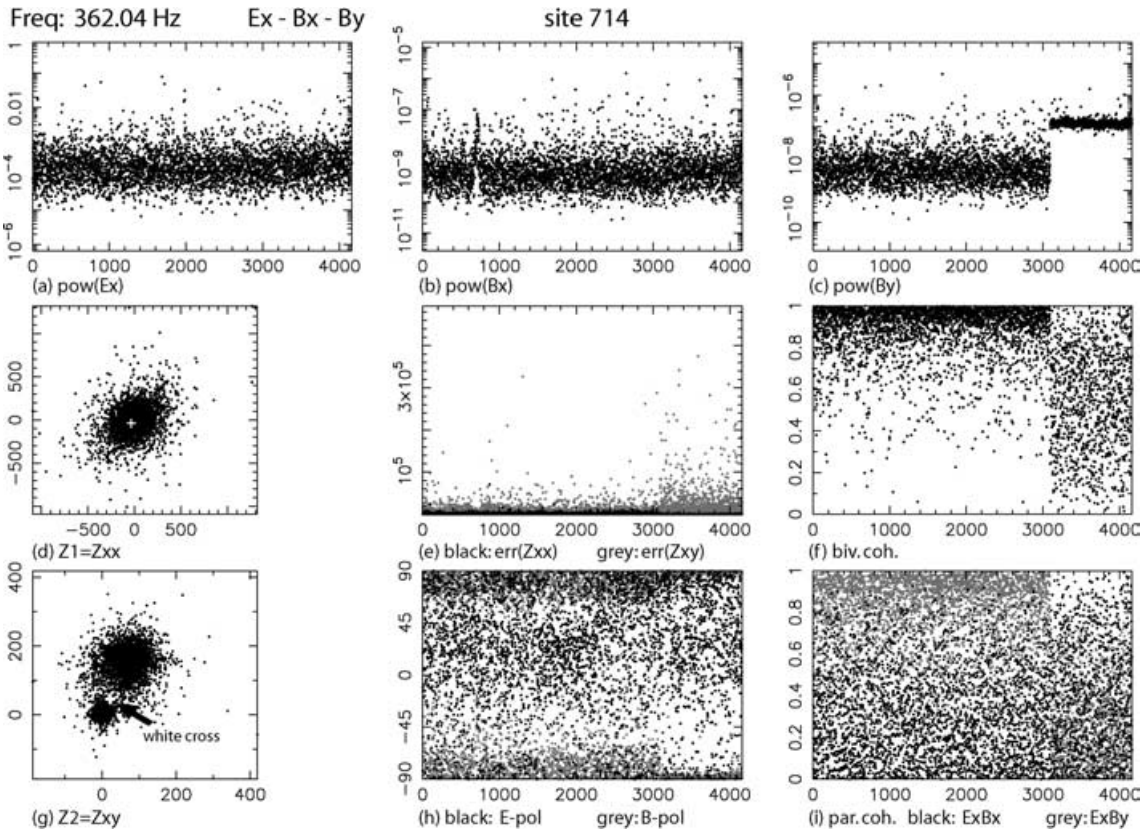

Figure 3. Data selection for 362.04 Hz and channels E_x, B_x and B_y of site 714. The spectral power density of B_y (c) indicates a distinct change in power for events greater than 3000, which is is accompanied by lower bivariate coherences (f). The distribution of the response function estimates Z_{xy} (g) exhibits two clusters. The white crosses in windows (d) and (g) indicate the mean values of the response functions computed on the basis of all accepted autospectra and cross-spectra.

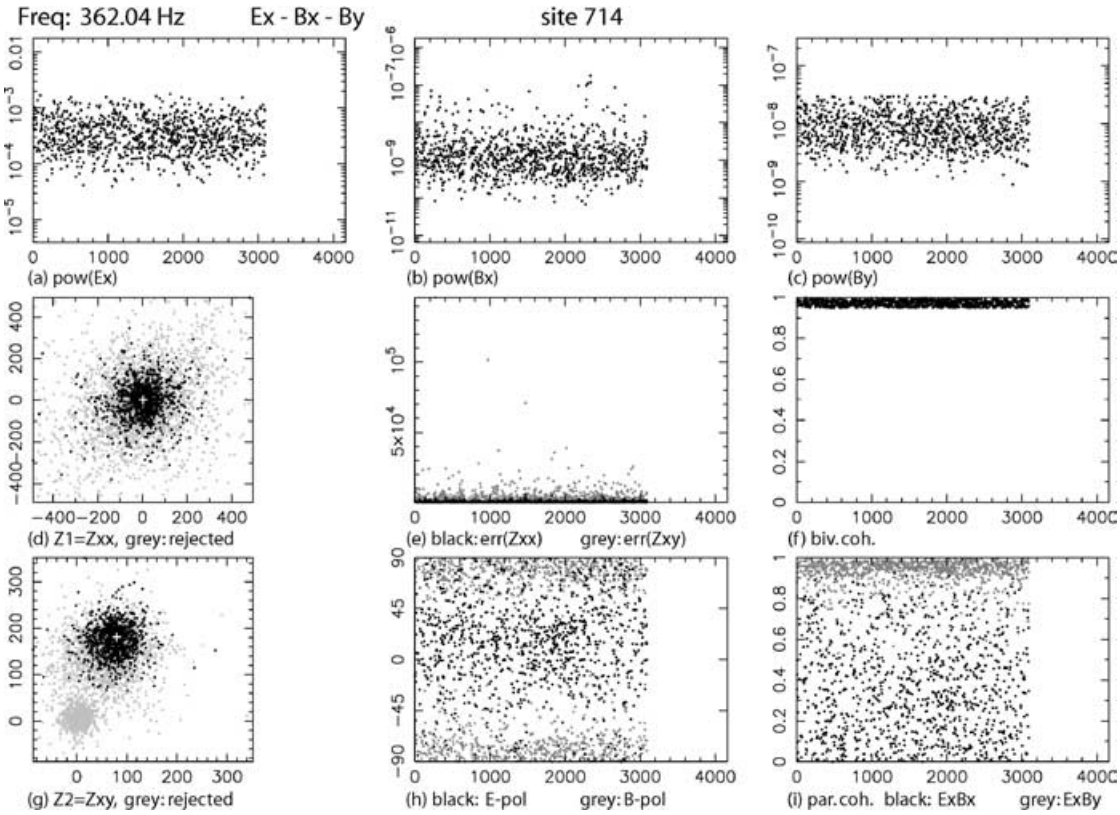

Figure 4. After rejecting events with bivariate coherences smaller than 0.95 (f), only one cluster for Z_{xy} (g) remains. The mean value of the transfer function (90; 190) km s^{-1} is marked by the white cross. The light grey dots in windows (d) and (g) show events that are rejected for the subsequent robust processing. This example describes the simple case of a data selection using coherence thresholds.

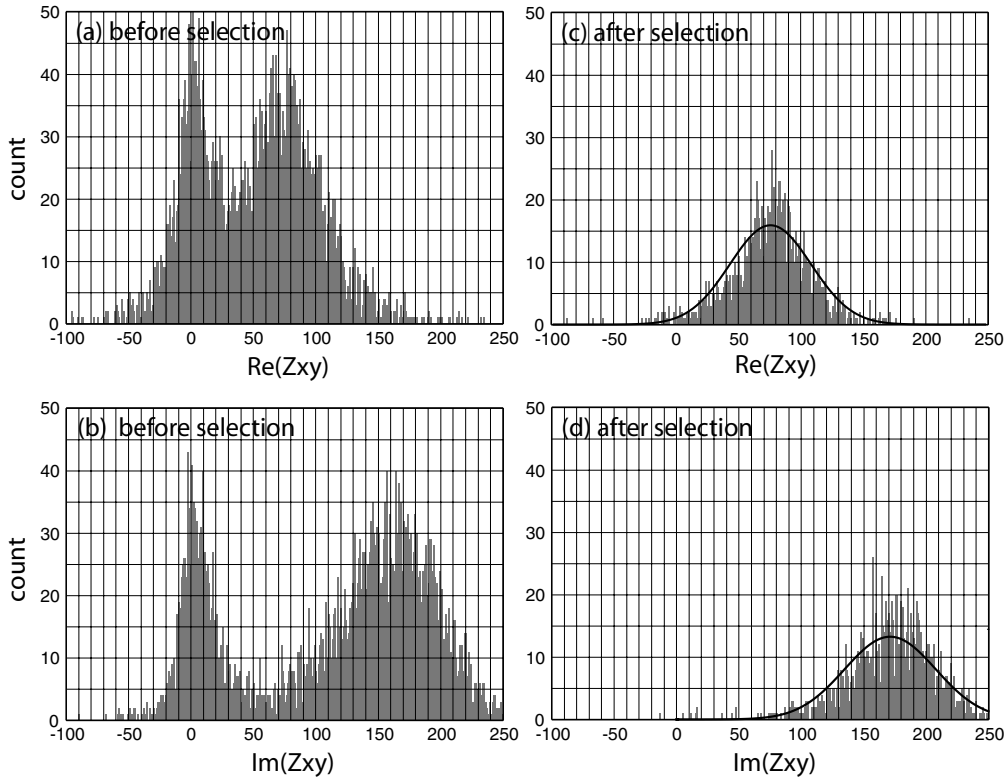

Figure 5. Histograms showing the distribution of $Re(Z_{xy})$ and $Im(Z_{xy})$ before (a and b) and after frequency domain selection (c and d). In graphs (a) and (b), we clearly see the two clusters shown in the complex plane in Fig. 3(g). After selection, only one cluster is left. Its circular shape in the Argand plot in Fig. 4(g) actually represents an approximate Gaussian distribution, which is shown as solid black line in graphs (c) and (d).

third quadrant for Z_{yx}. Applying the phase criterion together with the coherence threshold to all frequencies prior to a subsequent robust single site reprocessing results in the smoothly varying apparent resistivity and phase curves for site 714 shown in Fig. 2(b). We found that many sites can be improved considerably using these two criteria and both can easily be applied in an automatic fashion. In order to check whether the resulting apparent resistivity and phase curves are both theoretically and statistically consistent, we applied the D+ algorithm and the Sutarno phase smoothing available within WINGLINK (`http://www.geosystem.net`). The D+ smoothing finds a 1-D conductivity model that best fits both the apparent resistivity and phase of each off-diagonal component (Parker & Whaler 1981; Beamish & Travassos 1992). The Sutarno phase smoothing (Sutarno & Vozoff 1991) applies a Hilbert transform to calculate a consistent apparent resistivity curve from the observed phase curve. Both algorithms can be used to confirm that the apparent resistivity and phase curves are consistent. The solid lines in Fig. 2(b) show the D+ curves, which in general fit the observed data quite well.

However, it must be thoroughly tested if the application of the phase criterion is justified, as in some circumstances it can lead to seriously misleading results. Fig. 6(a) shows apparent resistivity and phase curves of a site in Namibia (094). As above, the data were pre-processed using the phase criterion and a coherence threshold. The *xy* apparent resistivity and phase curves appear largely undisturbed, except for some bias at around 0.1 Hz. The *yx* curves, on the other hand, are mostly unresolved (exhibiting scatter) for the lowest frequencies (<0.05 Hz). Fig. 7 shows the parameter distribution exemplarily for a frequency of 0.0884 Hz. The response functions Z_{yx} and Z_{yy} are estimated from E_x and both horizontal magnetic field components. In windows (d) and (g), we obtain circular clusters for each of the response functions. However, the Z_{yx} estimates in window (d) are partly located in the third quadrant, as expected for a simple subsurface structure, but to a large part also in the fourth quadrant. Eliminating one half of the data with the phase criterion results in a cluster that is no longer circular shaped; the underlying Gaussian distribution is thereby destroyed. Closer examination of data from this site reveals that all lower frequency Z_{yx} phase values leave their assigned quadrant. If solely the coherence criterion is applied for the data pre-selection, the smooth apparent resistivity and phase curves in Fig. 6(b) are obtained. Clearly, the phase curve of the *yx* component crosses very consistently two quadrants. This effect is caused by a complicated, 3-D subsurface structure, which is discussed in detail by Weckmann *et al.* (2003).

3.2 Coherent noise in the electric fields

In the previous two examples, it was shown that rather simple selection criteria could recover the intervals of undisturbed electromagnetic signals. These criteria are generally not valid or sufficient and other parameters, such as the magnetic field polarization directions, must be considered to distinguish between signal and noise.

Apparent resistivity and phase curves of another site in Jordan (727) are shown in Fig. 8(a). The *xy* components reveal strong disturbances in the frequency band between 2 and 0.05 Hz, while the *yx* components appear not affected by noise. We demonstrate the pre-selection procedure at a frequency of 1 Hz (Fig. 9). The power

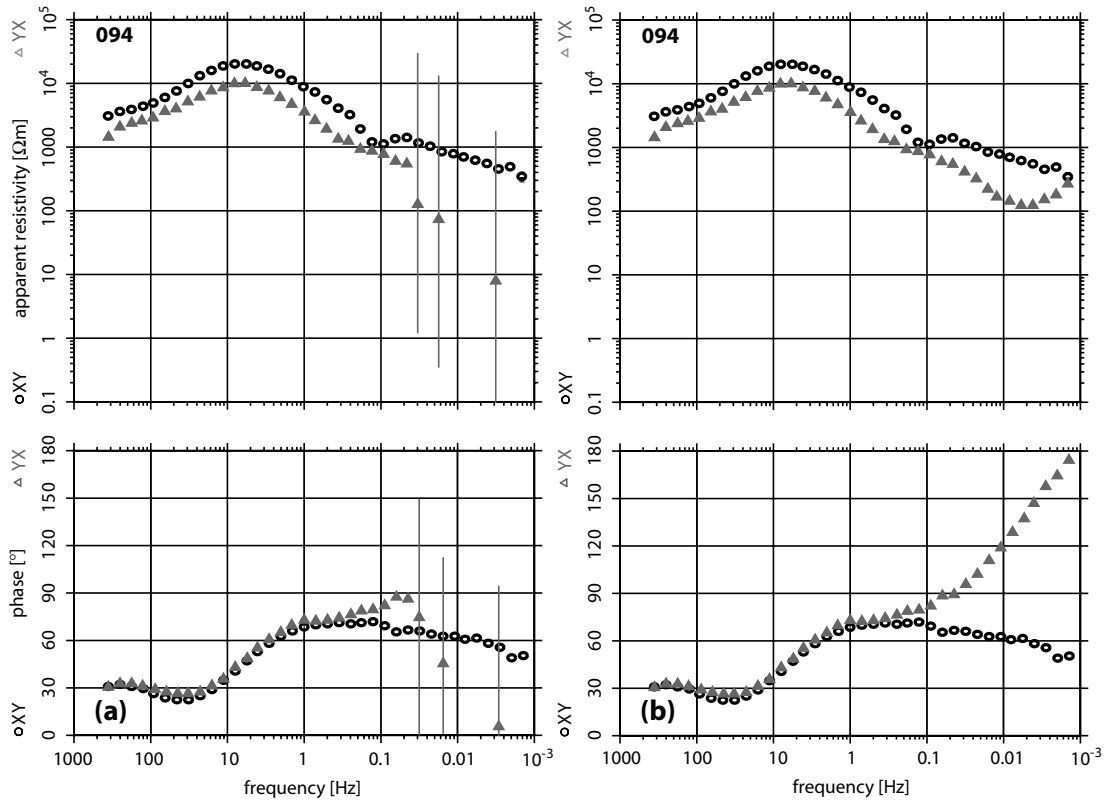

Figure 6. Apparent resistivity and phase curves of site 094 (Namibia) obtained from robust processing with automatically applied coherence and phase criterion (a). The *yx* component is poorly estimated for frequencies lower than 0.05 Hz. (b) Applying only the coherence criterion of 0.95 yields smooth and continuous curves with a phase transition from the first (0°–90°) into the second quadrant (90°–180°).

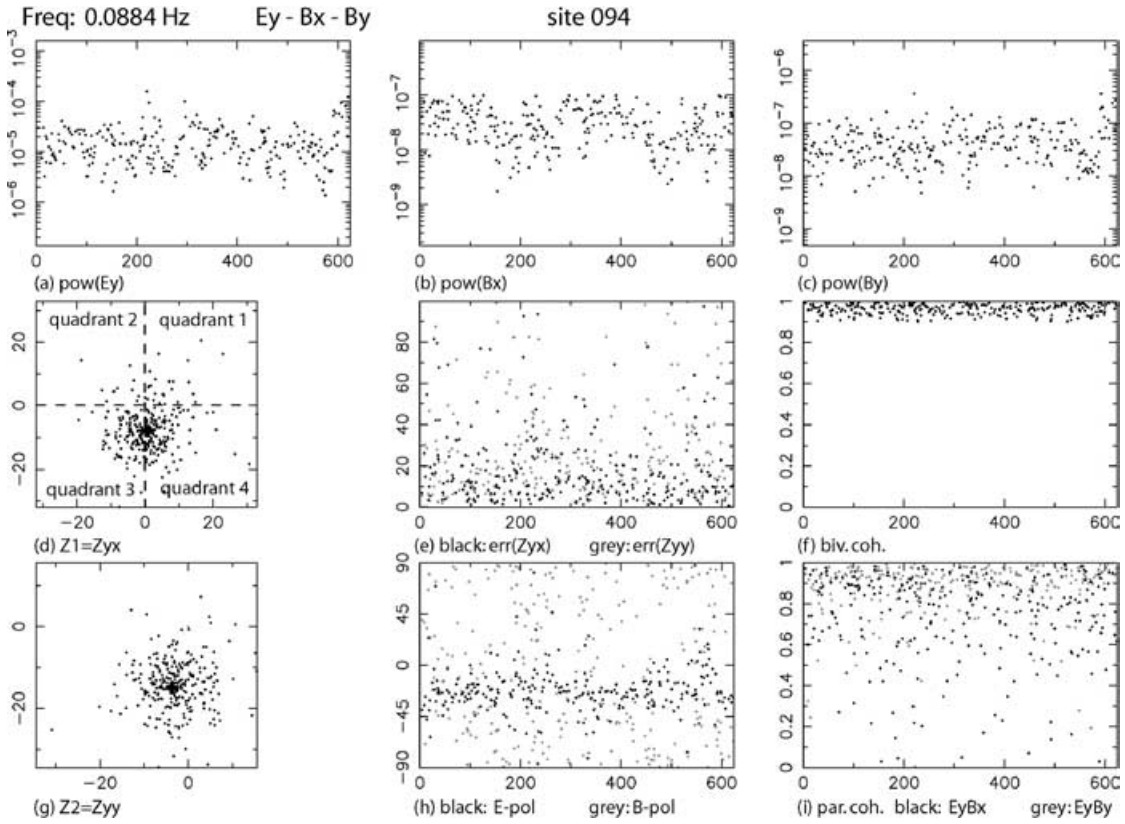

Figure 7. Displaying the distribution of response function estimates Z_{yx} (d) for 0.0884 Hz clearly shows that the position of the cluster is not confined entirely to the third quadrant of the complex plane. Applying the phase criterion destroys the Gaussian distribution by eliminating one half of the cluster. The data set from Namibia is an example of a site influenced by strong 3-D effects, where the phase criterion must not be applied.

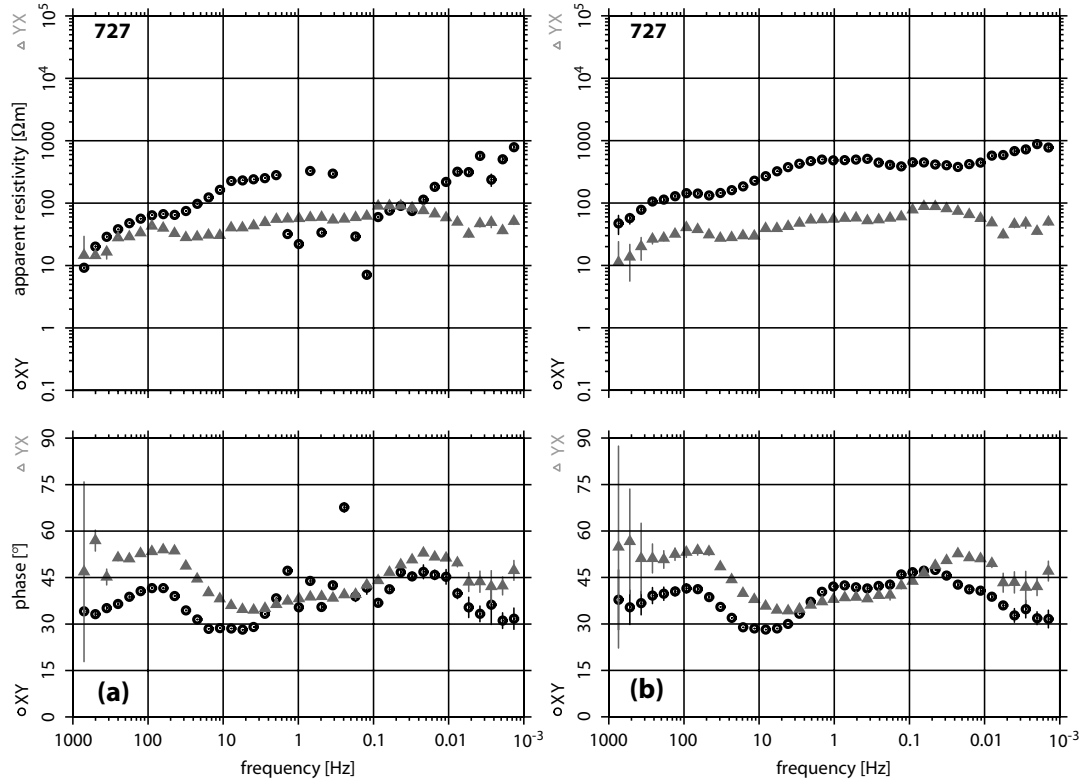

Figure 8. Apparent resistivity and phase curves of site 727 obtained from (a) applying the robust processing scheme and (b) applying the data pre-selection in combination with the robust processing.

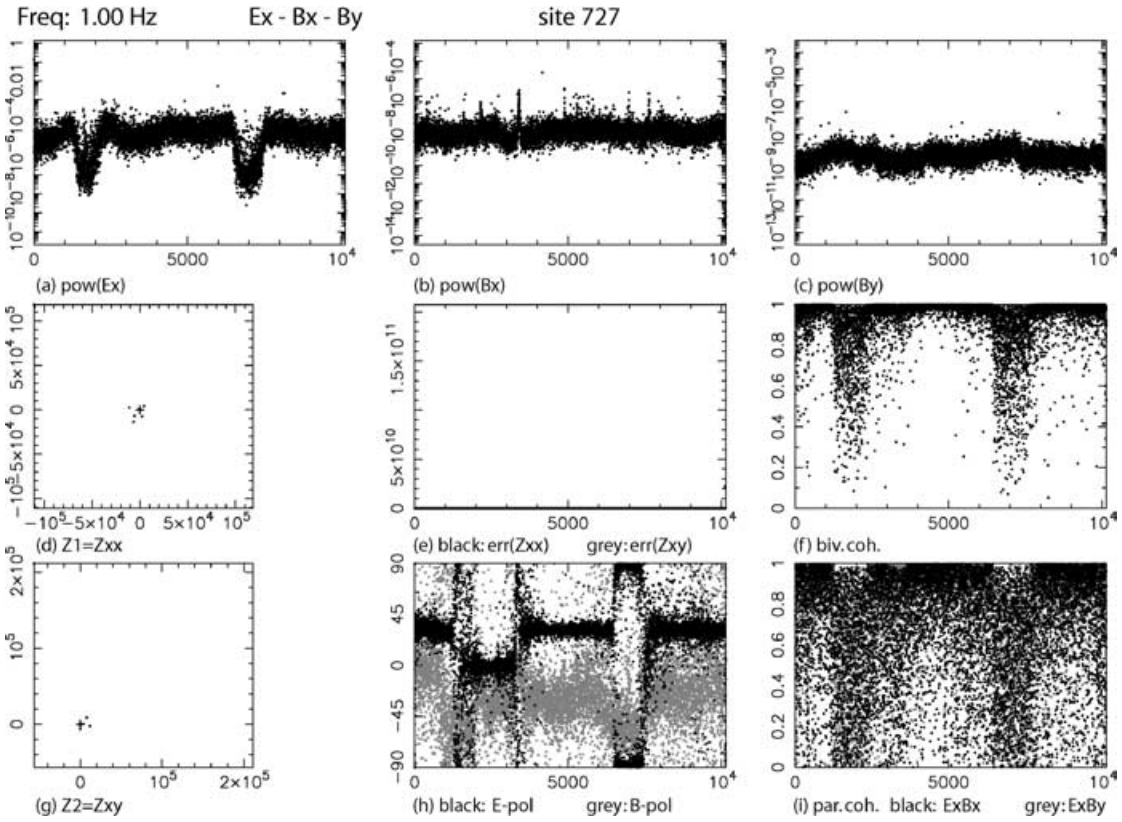

Figure 9. The spectral power density for 1 Hz of the output channel E_x (a) exhibits two kinks of low power. They correlate with lower bivariate coherences (f) and a change in electric polarization direction (black in h). Note that the scaling of the axes in graphs (d), (e) and (g) depends on the respective minimum and maximum values.

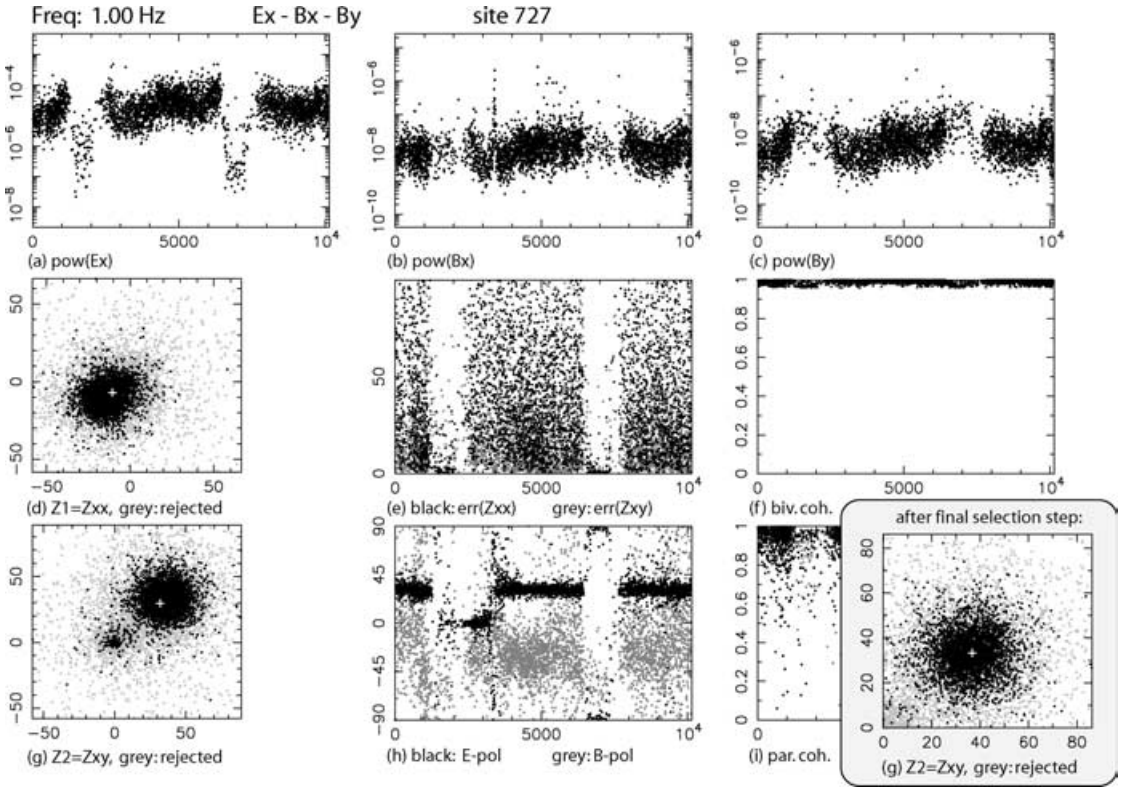

Figure 10. After rejecting events with bivariate coherences (f) lower than 0.95 and response function errors (e) larger than 100 km s^{-1}, mostly events with high power are left. A few remaining events with lower power cause the second small cluster for Z_{xy} (g), which shifts the averaged response function (white cross) towards the smaller cluster. After rejection of all low-power events, an undistorted transfer function (inset g) is obtained.

density of E_x (a) reveals two distinct time intervals, both approximately 500 events wide, showing a drastic drop in the power of more than two decades. This behaviour is not observed in the magnetic channels in windows (b) and (c). The decreases in power of channel E_x correlate with lower bivariate coherences (f) and also with changes in electrical polarization directions (h). For most time spans, we observe fairly strong electric field polarization directions of approximately 30–40°, but for the above mentioned intervals they change to 0° or ± 90° (h). The cluster of response function estimates and their errors in windows (d), (e) and (g) are hardly visible as the automatic axis scaling adjusts to some very large outliers in the data.

As a first step, we assume that only events with high bivariate coherence result in the correct response function estimates. Hence, we apply a minimum threshold value of 0.95 for the coherence and, in addition, we reject all data with response function errors larger than 100 km s^{-1} (see Fig. 10). The latter does not introduce a major cut in the error distribution, as it merely removes some of the worst outliers. Fig. 10 shows the data set after this first selection step (note the change in axes of many graphs). As a consequence of the thresholds, some of the low-power events in E_x were also removed. Now, we can recognize the distributions of both response functions in Figs 10(d) and (g). Z_{xx} (d) exhibits a circular distribution but the location of the cross (mean value of the distribution) is off-centre indicating that some events still bias the average. For the Z_{xy} response function in window (g), we observe two clusters. By examination of the impedance tensor data versus event numbers (not shown), it becomes obvious that the remaining low-power events are responsible for the smaller cluster. After removing events with power density lower than 10^{-6}[mV^2 km^{-2} Hz^{-1}] in E_x, we derive an average response function (white cross), which is located in the centre of the larger cluster (inset of Fig. 10g).

In this example, noise was mostly affecting one component of the electric field but, contrary to the common expectation, the noisy intervals were marked by smaller than average electric field spectral power densities. The disturbed events showed lower coherences and higher response function errors when compared with the undisturbed time spans. Approximately 35 per cent of the data were rejected (3358 events from a total of 10 145 at a frequency of 1 Hz) but the inclusion of this amount of disturbed data is sufficient for the robust stacking to fail. After removal of these bad data, the robust stacking can recover the undisturbed apparent resistivity and phase curves (see Fig. 8b). For the lowest frequencies (<0.002 Hz), however, there were too few events recorded for successful application of the pre-selection scheme.

3.3 Strongly polarized source fields

The next example shows data from a site in Jordan (705) located within the military zone, approximately 20 km away from the previous site (727). The MT data in Fig. 11(a) exhibit disturbed apparent resistivity and phase curves between 1 and 0.02 Hz for both components. As the scatter is larger on the *yx* component, particularly the phases, we will demonstrate the selection scheme for the combination of channels E_y, B_x and B_y at a frequency of 1 Hz.

Fig. 12 shows the distribution of the MT parameters after applying thresholds of 100 for the errors of both transfer functions and 0.95 for the coherence. The resulting distribution of the spectra power density

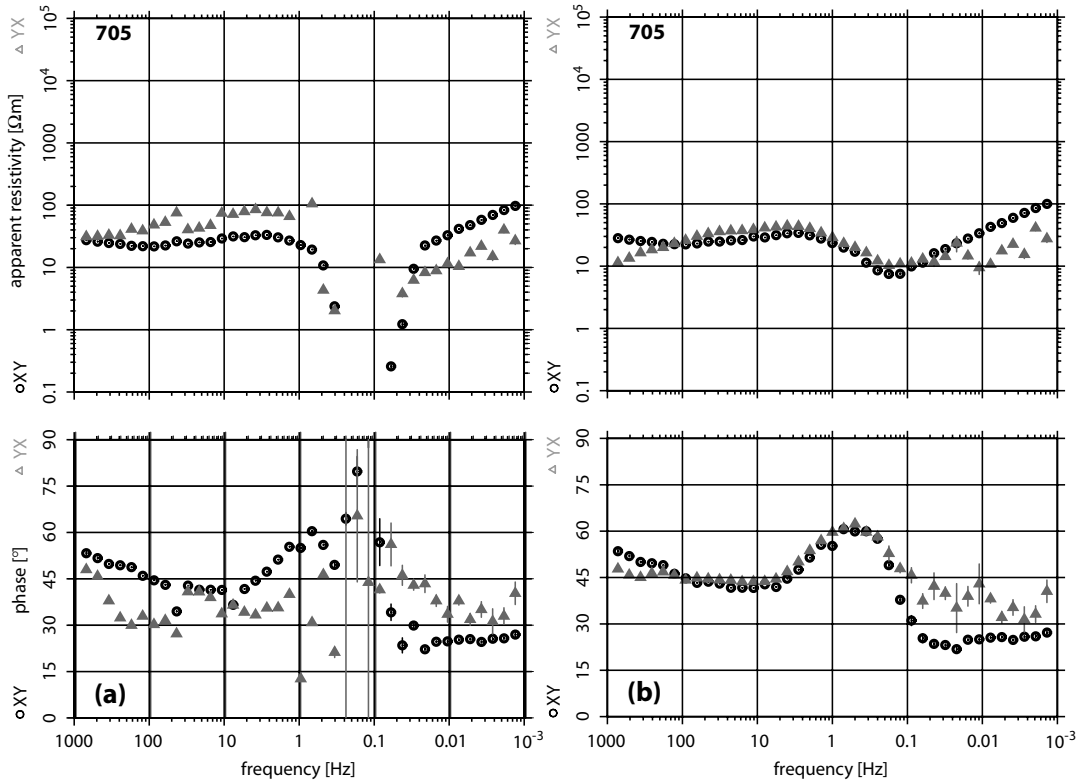

Figure 11. Apparent resistivity and phase curves of site 705 obtained from applying the robust processing scheme (a). Both curves are severely biased between 1 and 0.02 Hz. The *yx* component reflects poor data quality over the entire frequency range. Applying data pre-selection in combination with the robust processing improves the results significantly (b) except at lower frequencies where the recordings of undisturbed time-series are too short to obtain enough low-frequency events.

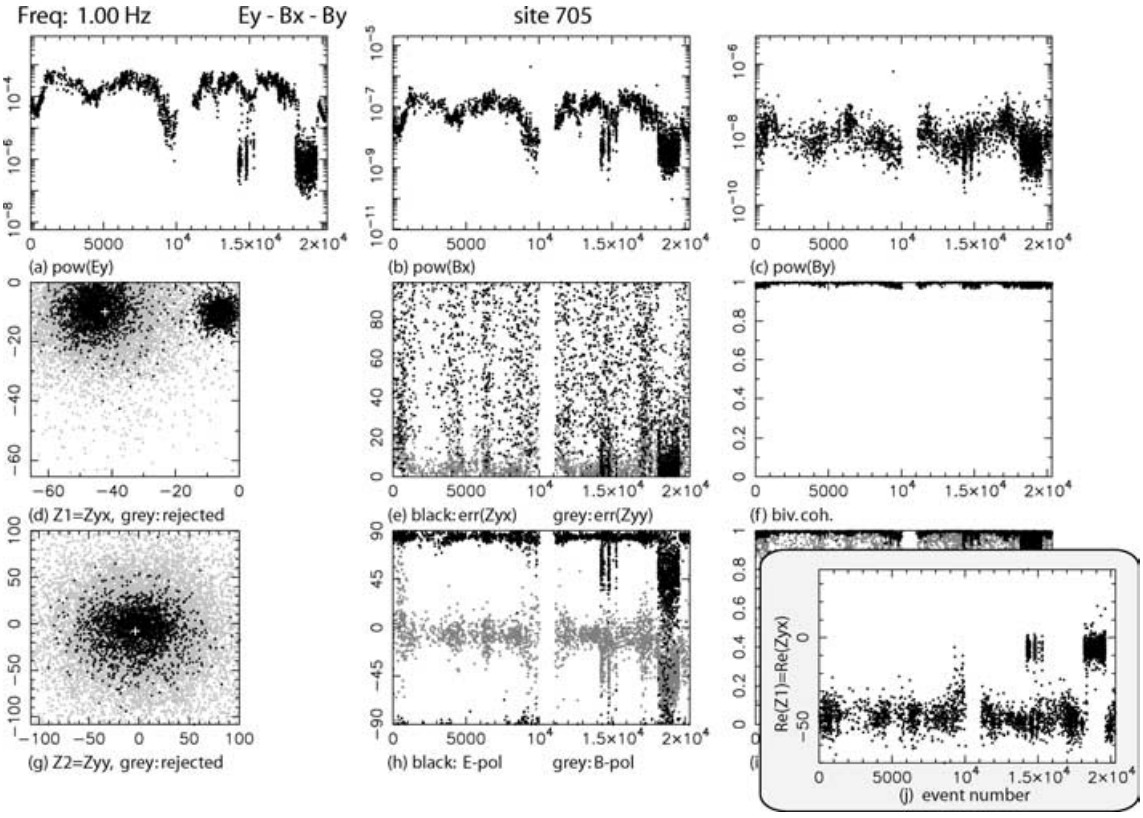

Figure 12. Applying a threshold of 100 km s^{-1} to the statistical response function errors (e) and a threshold value of 0.95 to the bivariate coherence (f) reveals the existence of two response function clusters Z_{yx} in graph (d) at site 705 for 1 Hz. The real part of Z_{yx} versus event number (inset j) shows an unambiguous correlation between high-power events and $Re(Z_{yx})$ values of ∼50 km s^{-1} and low-power events and $Re(Z_{yx})$ values ∼10 km s^{-1} for the real part of Z_{yx} estimates. Although we can identify high and low values of the spectral power density of E_x (a) and the response function errors as well as different electric and magnetic polarization directions (h), the bivariate coherences are high for all remaining events and do not exhibit differences observed in various other statistical parameters.

of E_y (a) and B_x (b) reveals intervals with distinctively lower than average power, similarly to our observations for E_x at site 727 (see Fig. 9a). At site 705, however, the pattern of lower power is visible in all three components, although to a much smaller extent in B_y. The distribution of the resulting response function estimates [Z_{yx} in window (d)] clearly separates into two clusters. Examination of the response function over time (inset Fig. 12j), reveals that high-power events are responsible for the cluster on the left. Note, however, both clusters consist of events with only very high bivariate coherence (f).

It is the distribution of the magnetic field polarization directions (h) and the response function errors (e) that suggest that the smaller cluster in window (d) gives the true response function. Naturally induced magnetic fields usually do not show a single preferred polarization direction as they are generated by various sources, such as the auroral and equatorial electrojets or Sq. Strongly polarized horizontal magnetic fields are typical for cultural noise sources (Szarka 1988). In this case, however, the intervals with variable magnetic field polarizations clearly correlate with the low-power events. For these time spans, the response function errors are also consistently smaller (e). Another indication for the noise being attributed to high power is the rather narrow power band of E_y (a) and B_x (b) and the abrupt drop in the power levels. Contrary to site 727, where levels of low spectral power density correlate with noisy data segments, we now have an opposite example where the low-power events lead to the undisturbed response function estimate.

The response function errors become small if the bivariate coherence is close to 1, and if the denominators in eqs (12) and (13) are large. The first part is fulfilled as all events in Fig. 12 have a coherence greater than 0.95. The denominator becomes very small, however, if noise is correlated on the orthogonal components B_x and B_y (Figs 12b and c). This is the case for the high-power events. Fig. 13 shows the remaining 926 events from a total of 20 324 (or 4.5 per cent of the data) if all data with a response function error >10 are rejected. The remaining response function estimates accumulate in one cluster with the average (white cross) in its centre (Fig. 13d). If the rest of the disturbed frequencies is treated in the same way, we obtain the apparent resistivity and phase curves of Fig. 11(b). Clearly, the the data quality has improved significantly. The *yx* component apparent resistivity and phase values at frequencies lower than 0.09 Hz could not be improved as only two short intervals, corresponding to 4 h recording time, could be used for the subsequent robust processing.

3.4 Further complications

Another site (744) is located close to a small village. Here, the apparent resistivity and phase curves (Fig. 14a) are disturbed between 0.7 and 0.09 Hz in the *xy* component and also between 128 and 16 Hz in the *yx* component. Closer inspection of the *yx* component data at a frequency of 32 Hz results in the parameter distribution shown

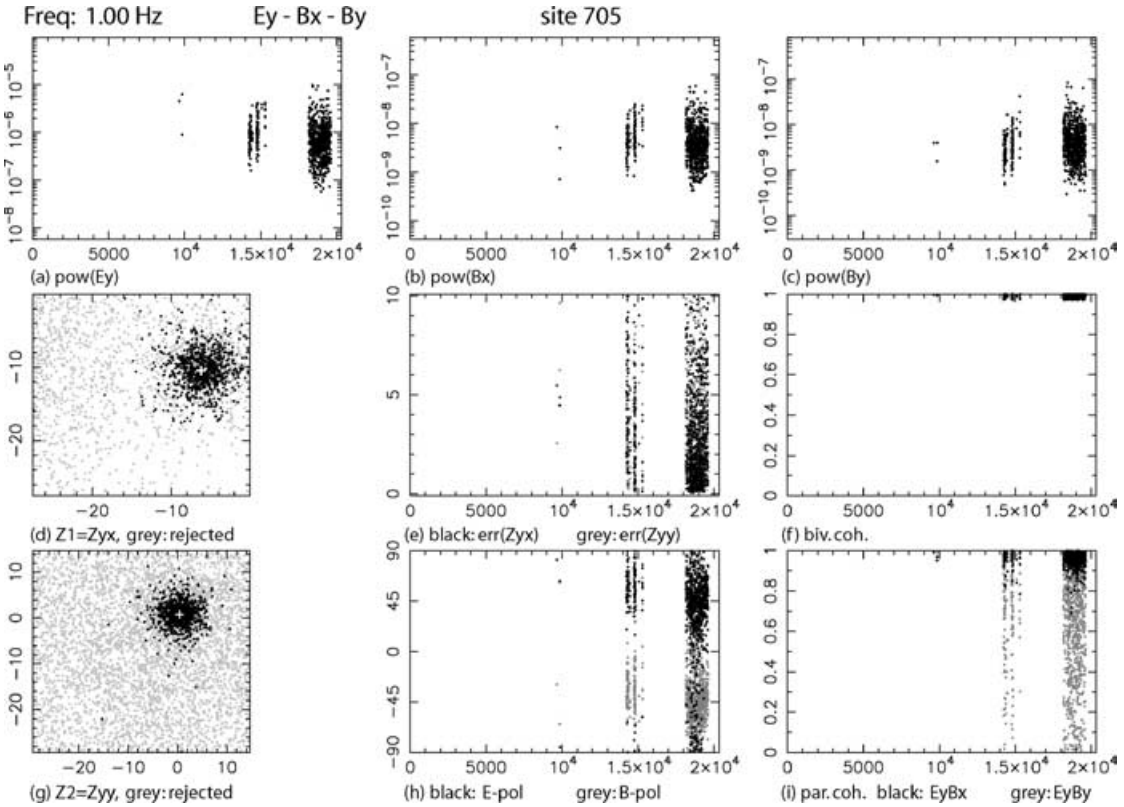

Figure 13. Rejecting events with response function errors (e) larger than 10 km s^{-1} results in one single transfer function cluster Z_{yx} (d) (see Fig. 12). In this example, the low-power events lead to the undisturbed response function estimate.

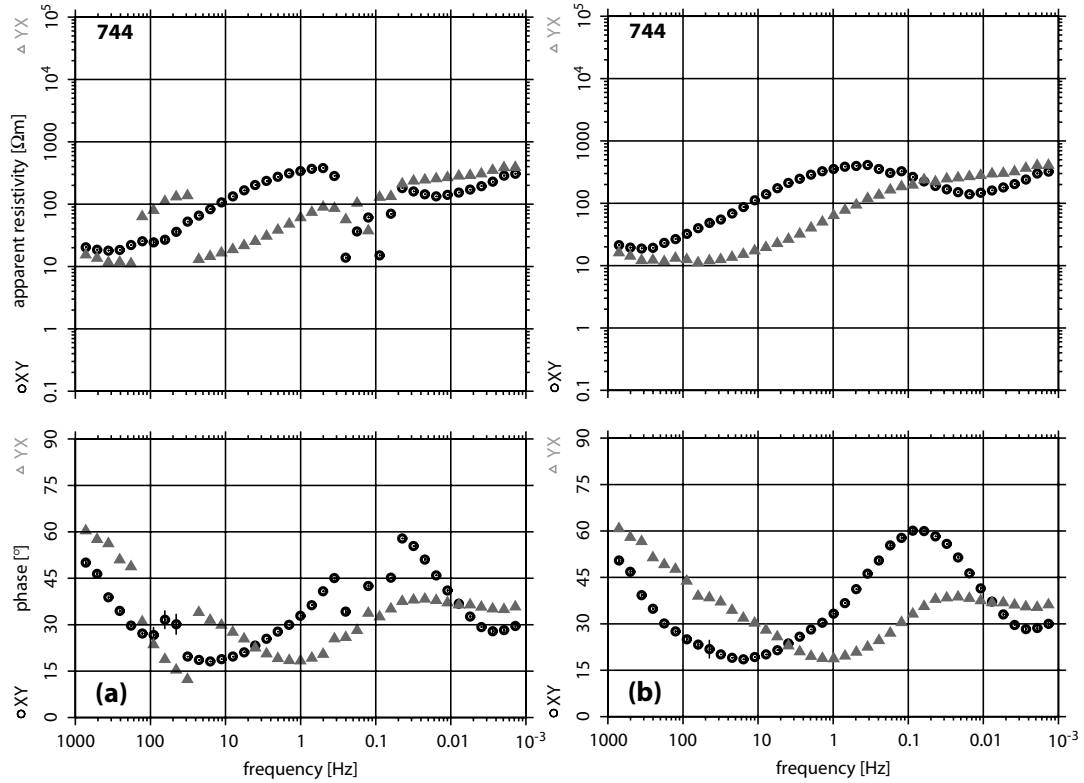

Figure 14. Apparent resistivity and phase curves of site 744 obtained from robust processing (a). The *yx* component reveals poor data quality in the frequency range from 0.8 to 0.09 Hz, but also between 128 and 16 Hz. (b) Applying frequency domain pre-selection in combination with the robust processing results in smooth curves over the entire frequency range.

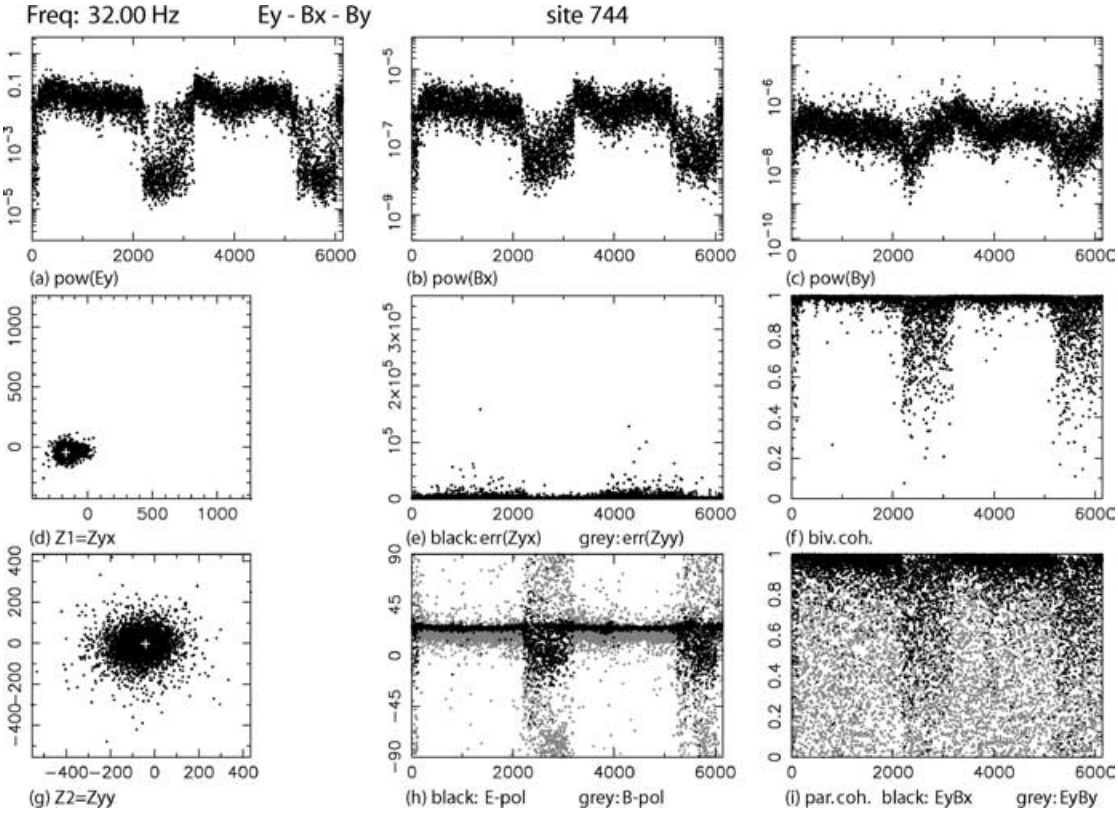

Figure 15. Main screen of magnetotelluric (MT) parameters at 32 Hz showing channels E_y, B_x and B_y at site 744. The spectral power density of E_y (a) at site 744 for the frequency of 32 Hz shows similarities to the spectral power density variation of E_x at site 727 (see Fig. 9a). Again, two response function clusters of Z_{yx} (d) can be observed as well as a change in the electric and magnetic polarization directions (h). In contrast to site 727, the low-power events correlate with lower bivariate coherences (f).

in Fig. 15(a). Again, we can distinguish between two high-power and two low-power intervals, showing a difference in power of more than two decades in E_y (a) and B_x (b) and somewhat less in B_y (c). Contrary to the last example (site 705 in Fig. 12), the variations of the spectral power densities of the high-power events appear natural as the power varies smoothly but with the expected spread, i.e. showing a daily variation. In this case, low-power events correlate with low bivariate coherences (f) but also with a larger variability of the magnetic polarization directions (h). Most parts of the other data segments show strongly polarized magnetic field directions of $\sim 25^\circ$. The response function cluster of Z_{yx} (d) appears to be smeared out but the white cross is located close to the centre of this distribution.

If we apply a bivariate coherence threshold of 0.95, many of the low-power events are rejected, discernable in window (a) of Fig. 16. Now, two clusters of Z_{yx} show up in window (d). The larger cluster on the left, representing the majority of events, is associated with the high signal power. As before, the response function errors (e) together with the magnetic polarization directions (h) are crucial to distinguish between noise and natural electromagnetic signal.

Applying an error threshold of 100 as the next selection step in Fig. 17 omits most of the high-power events but the accepted number of low-power events remains the same (a). The distribution of response function errors in window (e) of Fig. 17 indicates that the low-power events have consistently smaller errors. So, quite as expected and hoped for, the response function errors are useful indicators for noise. Large errors are caused if high power in E_y, if not matched by similarly high power in B_x and B_y and/or if noise is correlated between the horizontal magnetic fields. The first results in a large numerator and the latter in a small denominator in eq. (13). Note however, that although the majority of the remaining data clearly centres around the cluster of the low-power events (d) this is not reflected by the mean value of the response function estimates as the position of the white cross is clearly biased towards the response function estimates of the high-power events.

If all all high-power events are removed by setting a threshold value of $2.0 \cdot 10^{-3}$[mV^2 km^{-2} Hz^{-1}] for the spectral power density of E_x (a), only one response function cluster is left. In this case, only 3.6 per cent of the available data is considered useful for the subsequent processing stages. However, using a similar strategy for the remainder of disturbed frequency bands results in the smooth and consistent apparent resistivity and phase curves shown in Fig. 14(b).

These last three examples showed some similarities as the spectral power densities of the output channels (E_x or E_y) partitioned into different amplitude levels for certain time segments. However, universally valid rules for a noise separation could not be derived as there is no particular consistently preferred power level. We rather have to investigate a combination of MT parameters, such as the transfer function errors and the magnetic polarization direction, to find the undisturbed response function estimates.

3.5 Vertical magnetic field processing

So far, we have discussed only MT cases with electric fields as output channels. However, the data selection scheme can be equally useful

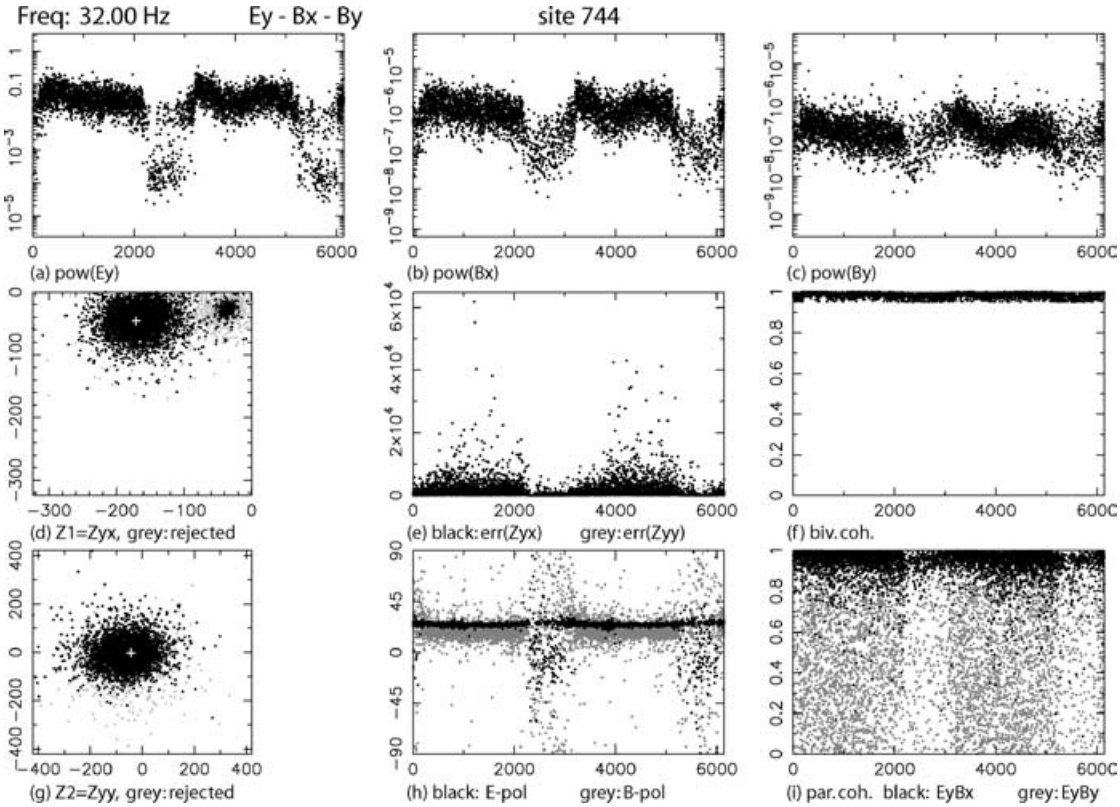

Figure 16. After rejecting events with bivariate coherences (f) lower than 0.95, it becomes obvious that the low-power events correlate with smaller response function errors. Additionally, very distinct magnetic polarization directions (h, grey dots) correlate with high-power events. Here, the few low-power events lead to undisturbed response function estimates.

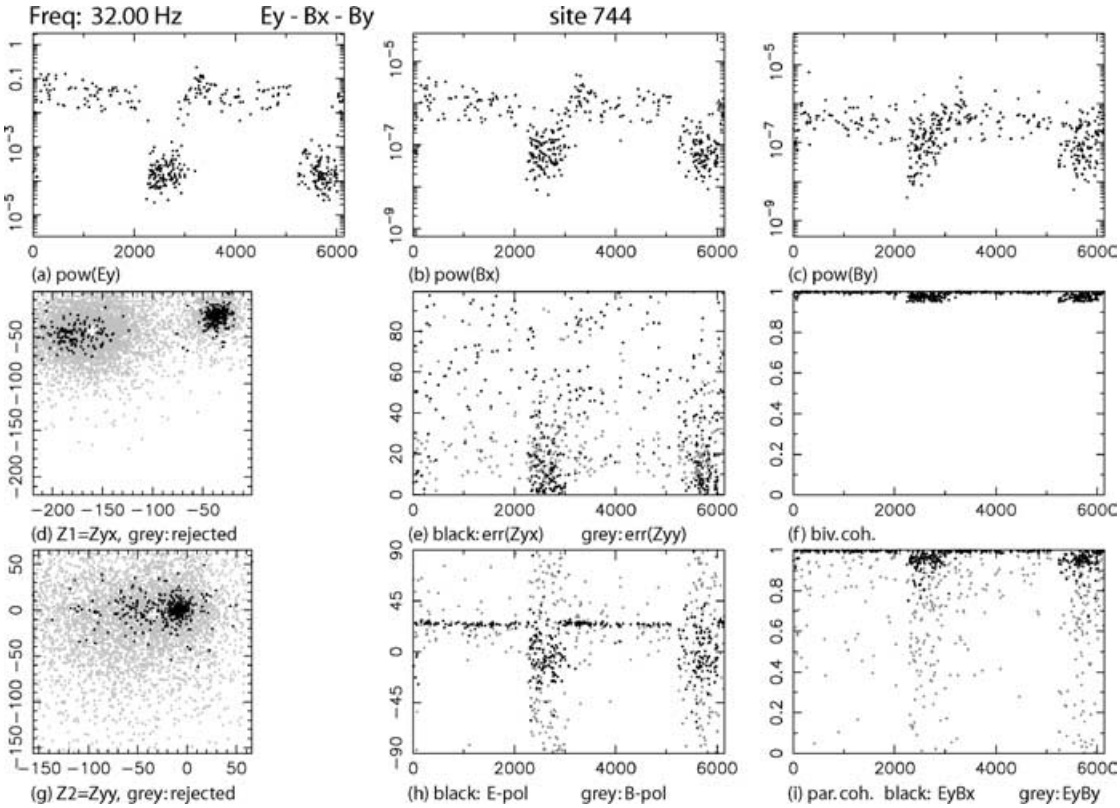

Figure 17. Applying a threshold of 100 km s^{-1} to the statistical response function errors (e) results in a rejection of most of the high-power events whereas the low-power events are not affected (compare Fig. 16).

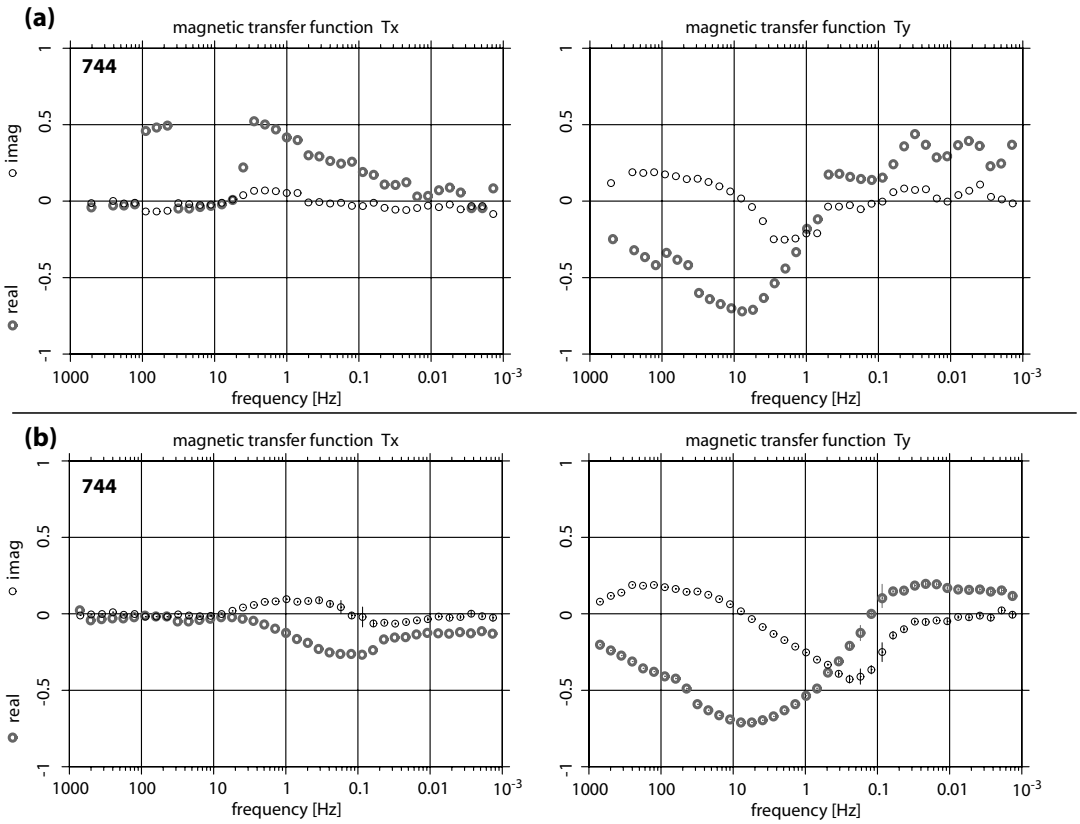

Figure 18. Magnetic transfer function of site 744 obtained from robust processing (a). The real part of T_x shows some sort of noise contamination, however a maximum of the $Re(T_x)$ curve of the order of 0.5 at 10 Hz is indicated. Applying data pre-selection with subsequent robust processing leads to different curves for the real part of T_x. In the frequency range, the response function showed a maximum of 0.5, the curve exhibits now a much smaller kink in the opposite direction (change of sign).

for calculating the geomagnetic response functions, as the vertical magnetic field can also be severely affected by noise. Contrary to the MT cases though, a phase criterion cannot be applied as there is no specific phase relation between horizontal and vertical magnetic fields.

We examine the same site as before (744) but now for another frequency band (2.8 Hz) and with respect to the magnetic response functions. At first glance, only the real part of T_x in Fig. 18(a), appears to be noisy as the curve is discontinuous in the frequency range between 36 and 2.8 Hz and also for the frequencies above 100 Hz. Comparing this response with those of neighbouring sites, however, reveals that only the T_y values are consistent but not the relatively large positive T_x values, which occur only at site 744. Fig. 19 shows the statistical properties after applying a bivariate coherence threshold of 0.95. The magnetic polarization directions (h) show one preferred polarization direction between 0° and 30° for the first 20 000 events, whereas the last 20 000 events exhibit no preferred polarization directions. Although the electric field polarization directions are not relevant for the calculation of the geomagnetic transfer functions, we can similarly distinguish between two intervals: 30° for the first half of the recording time compared with 0° to −30° for the second half. The response function errors of T_x (e) also differ between the first and the second half of the recording interval. The distribution of response function estimates T_x and T_y in windows (d) and (g), on the other hand, appear as a single cluster in each case.

At this stage, we can only presume that the much greater variability in the magnetic field polarization directions could indicate that the second half of the data set is the result of natural signal activity. To test this hypothesis, we first reject the second half of the data (all events with an event number greater than 20 000). As a result, we obtain one cluster for T_x with average values of 0.5 for the real part and approximately 0.0 for the imaginary part (Fig. 20d). This estimate fits the T_x curve shown in Fig. 18(a), which reaches its maximum value at around 10 Hz. Obviously, the events of the first half of recording interval have also dominated the robust processing. If we start over again but this time keep the other part of the data (reject all event numbers smaller than 20 000), we obtain a cluster for T_x with an average close to 0.0 for both, real and imaginary parts (Fig. 21d).

If we apply both strategies to all affected frequencies, we obtain two different but very consistent and smooth curves over the entire frequency range: one with a maximum of 0.5 at around 10 Hz and another curve that is close to 0.0 over most of the frequency range. However, only the latter curve is consistent with the neighbouring sites, which are located approximately 1 km further to the east and west. This consistent response is shown in Fig. 18(b). The magnetic response functions obtained from the first half of recording interval are likely showing the near-field effects of a nearby electromagnetic source. It is interesting to note that although both parts of this data set contain approximately the same number of events, the robust

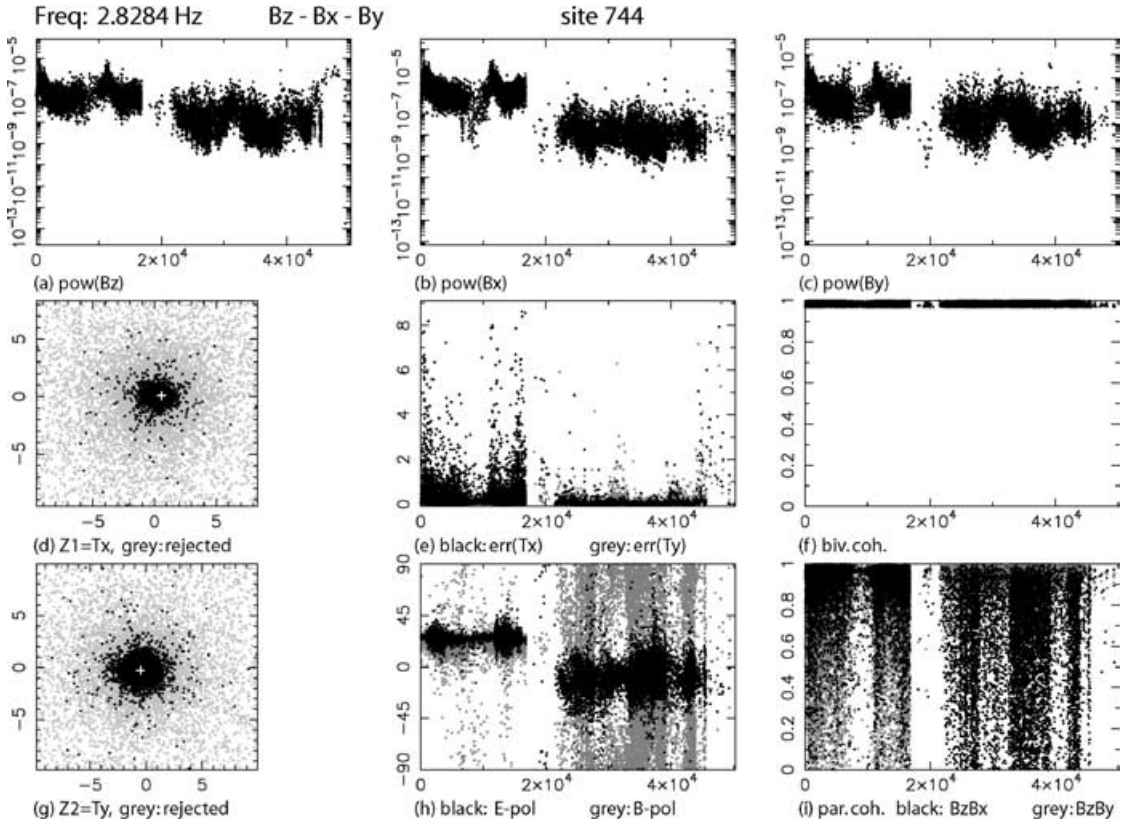

Figure 19. We can identify two different levels of spectral power density of B_z (a) for the first and the last 20 000 events for the magnetic fields at site 744. Additionally, both sets show different magnetic polarization direction (h, grey dots). Events with bivariate coherences (f) lower than 0.95 are already rejected.

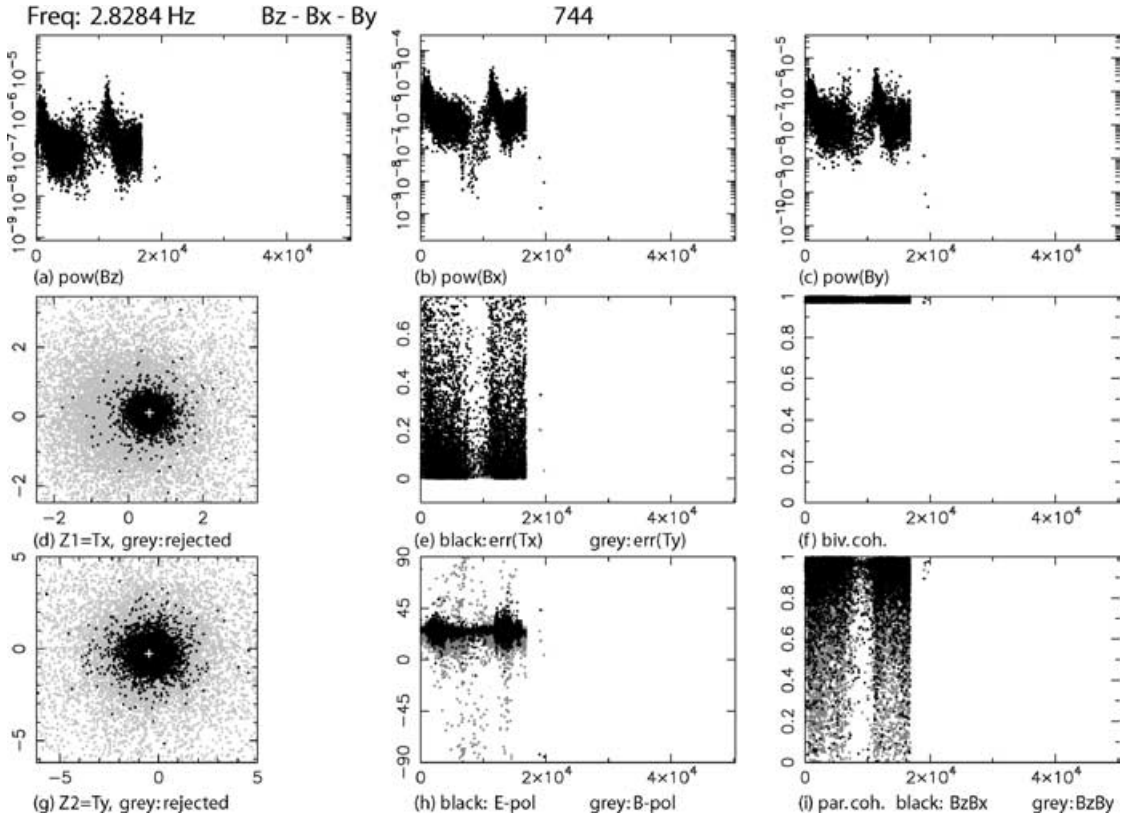

Figure 20. Accepting only the first 20 000 events results in a geomagnetic response function T_x (a) with 0.5 for the real part and approximately 0 for the imaginary part. This subset of events has dominated in the robust processing scheme. Applying the pre-selection scheme to all disturbed frequencies leads to a smooth curve with a maximum of 0.5 at 10 Hz.

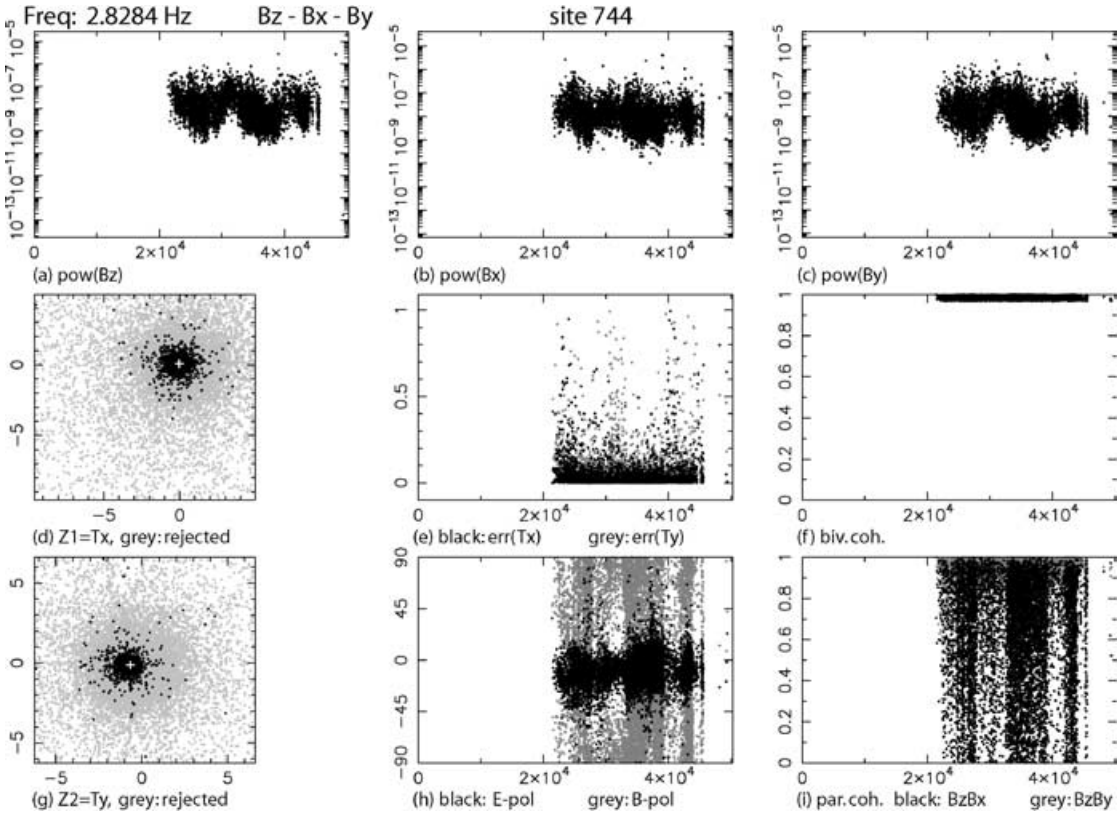

Figure 21. Accepting only the last 20 000 events results in a geomagnetic response function T_x (a) with a real part and imaginary close to 0. Applying this selection criterion to all frequencies, we obtain the geomagnetic response function curves shown in Fig. 18(b). Only this result is consistent with the results from neighbouring sites.

processing decides in favour of the first half and does not produce estimates that are an average of the two distributions.

4 CONCLUSIONS

In this paper, we demonstrate that a data pre-selection scheme in the frequency domain together with subsequent single site robust processing are an effective tool for signal/noise separation. Typically, all observed electromagnetic field components are contaminated to some extent with noise. The outcome of automatic data processing schemes will therefore often be disappointing, if robust single site processing or even robust remote reference procedures are applied. The remote reference method cannot always improve the results, as a successful application requires additional horizontal magnetic field components of a remote site without correlated noise. Often such a remote site is not available and we are faced with single site robust processing. Robust least-square algorithms in general work under the assumption that noise is a minor fraction of the total signal and particularly the input channels are free of noise. However, our examples clearly show that the magnetic channels are also influenced by noise and even orthogonal magnetic components contain a correlated noise signal.

With the frequency domain selection approach presented in this paper, undisturbed events can be identified without the aid of reference magnetic fields. This data pre-selection scheme is based on displaying nine different statistical MT parameters simultaneously over recording time. Data examples from Jordan and Namibia reveal that selection solely on the basis of the spectral power density or bivariate quadratic coherence can be misleading. Both a natural signal and noise can be related to high coherence values or have either high or low power. However, the statistical response function errors as well as the magnetic polarization directions can effectively help to distinguish between noise and a natural signal. A preferred direction of magnetic field polarization usually indicates a local noise source influencing the magnetic fields. In particular, if both magnetic field components contain correlated noise the response function errors become very large.

With the frequency domain selection, one aims to find a cluster of the true response function estimates. Extreme outliers or additional data clusters of response function estimates related to noise are removed, so that the remaining estimates form a circular-shaped distribution, which is expected for Gaussian distributed data.

Universally valid selection rules cannot be given, but by viewing and comparing various statistical MT parameters, we build knowledge on signal and noise properties of a given data set. Frequency domain editing is time consuming and in a reasonable expenditure of time it is best applied to a subset of frequency bands. Predefined thresholds for an automatic data selection can be applied, which is sufficient to deal with sites affected by moderate amounts of noise. However, sites with more severe noise influence have to be revised manually. Often only a few per cent of the entire amount of data are relatively free of noise, but these can lead to greatly improved apparent resistivity and phase curves after reprocessing. To retrieve unbiased response function estimates, long recording times are required to ensure that a sufficient number of good data are available for the reprocessing.

ACKNOWLEDGMENTS

UW was supported by the Emmy Noether fellowship of the German Science Foundation (DFG) (WE 2938/1-1). All MT data were recorded with instruments provided by the Geophysical Instrument Pool of the GeoForschungsZentrum (GFZ). We also thank Alan Jones, Xavier Garcia and an anonymous reviewer for their thoughtful comments on the manuscript.

REFERENCES

Beamish, D. & Travassos, J., 1992. The use of the d+ solution in magnetotelluric interpretation, *J. appl. Geophys.,* **29,** 1–19.

Berdichevsky, M., 1960. Principles of magnetotelluric profiling theory, *Appl. Geophys.,* **28,** 70–91.

Berdichevsky, M., 1964. Linear relationships in the magnetotelluric field, *Appl. Geophys.,* **38,** 99–108.

Boerner, D., Kurtz, R. & Craven, J., 1993. Orthogonality in csamt and mt measurements, *Geophysics,* **58**(7), 924–934.

Chave, A. D. & Thomson, D. J., 1989. Some comments on magnetotelluric response function estimation, *J. geophys. Res.,* **94**(B10), 14 215–14 225.

Chave, A. D. & Thomson, D. J., 2004. Bounded influence magnetotelluric response function estimation, *Geophys. J. Int.,* **157,** 988–1006, doi: 10.1111/j.1365–246X.2004.02203.x.

Chave, A. D., Thomson, D. J. & Ander, M.E., 1987. On the robust estimation of power spectra, coherences and transfer functions, *J. geophys. Res.,* **92,** 633–648.

DESERT Research Group, 2000. Multinational geoscientific research effort kicks off in the middle east, *EOS, Trans. Am. geophys. Un.,* **81,** 609, 616–617.

Egbert, G., 1997. Robust multiple-station magnetotelluric data processing, *Geophys. J. Int.,* **130,** 475–496.

Egbert, G. & Booker, J., 1986. Robust estimation of geomagnetic transfer functions, *Geophys. J. R. astr. Soc.,* **87,** 173–194.

Egbert, G. & Livelybrooks, D., 1996. Single station magnetotelluric impedance estimation: Coherence weighting and the regression *m*-estimates, *Geophysics,* **61**(4), 964–970.

Fisher, R., 1922. The goodness of fit of regression formulae, and the distribution of regression coefficients, *J. R. Stat. Soc.,* **85,** 597–612.

Fontes, S., Harinarayana, T., Dawes, G. & Hutton, V., 1988. Processing of noisy magnetotelluric data using digital filters and additional data selection criteria, *Phys. Earth planet. Int.,* **52,** 30–40.

Fowler, R., Kotick, B. & Elliot, R., 1967. Polarization analysis of naturally and artificially geomagnetic micropulsations, *J. geophys. Res.,* **72,** 2871–2883.

Gamble, T., Goubau, W. & Clarke, J., 1979. Magnetotellurics with a remote reference, *Geophysics,* **44,** 53–68.

Garcia, X. & Jones, A. G., 2002. Atmospheric sources for audio-magnetotelluric (amt) sounding, *Geophysics,* **67**(2), 448–458, doi: 10.1190/1.1468604.

Goubau, W., Gamble, T. & Clarke, J., 1978. Magnetotelluric data analysis: removal of bias, *Geophysics,* **43,** 1157–1166.

Hattingh, M., 1989. The use of data-adaptive filtering for noise removal on magnetotelluric data, *Phys. Earth planet. Int.,* **53,** 239–254.

Jenkins, G. & Watts, D., 1968. *Spectral Analysis and Its Applications,* Holden-Day, San Francisco.

Jones, A., 1979. On the difference between polarisation and coherence, *J. Geophys.,* **45,** 223–239.

Jones, A., 1980. Geomagnetic induction studies in scandinavia i. determination of the inductive response function from magnetometer array data, *J. Geophys.,* **48,** 181–194.

Jones, A. & Jödicke, H., 1984. Magnetotelluric transfer function estimation improvement by a coherence-based rejection technique. In: *54th Annual International Meeting, Soc. of Expl. Geophys.,* SEG, Georgia, Atlanta, USA, pp. 51–55.

Jones, A., Chave, A., Egbert, G., Auld, D. & Bahr, K., 1989. A comparison of techniques for magnetotelluric response function estimation, *J. geophys. Res.,* **94,** 14 201–14 213.

Junge, A., 1996. Characterization of and correction for cultural noise, *Surv. Geophys.,* **17,** 361–391.

Larsen, J., 1989. Transfer functions: smooth robust estimates by least-squares and remote reference methods, *Geophys. J. Int.,* **99,** 645–663.

Larsen, J., Mackie, R., Manzella, A., Fiordelisi, A. & Rieven, S., 1996. Robust smooth magnetotelluric transfer functions, *Geophys. J. Int.,* **124,** 801–819.

Müller, A., 2000. A new method to compensate for bias in magnetotellurics, *Geophys. J. Int.,* **142,** 257–269.

Oettinger, G., Haak, V. & Larsen, J., 2001. Noise reduction in magnetotelluric time-series with a new signal-noise separation method and its application to a field experiment in the saxonian granulite massif, *Geophys. J. Int.,* **146,** 659–669.

Parker, R. & Whaler, K., 1981. Numerical methods for establishing solutions to the inverse problem of electromagnetic induction, *J. geophys. Res.,* **86,** 9574–9584.

Pedersen, L., 1982. The magnetotelluric impedance tensor—its random and bias error, *Geophys. Prospect.,* **30,** 188–210.

Ritter, O., Junge, A. & Dawes, G. J., 1998. New equipment and processing for magnetotelluric remote reference observations, *Geophys. J. Int.,* **132,** 535–548.

Ritter, O., Ryberg, T., Weckmann, U., Hoffmann-Rothe, A., Abueladas, A., Garfunkel, Z. & DESERT Research group, 2003a. Geophysical images of the Dead Sea Transform in Jordan reveal an impermeable barrier for fluid flow, *Geophys. Res. Lett.,* **30**(14), 1741, doi: 10.1029/2003GL017541.

Ritter, O., Weckmann, U., Vietor, T. & Haak, V., 2003b. A magnetotelluric study of the Damara Belt in Namibia 1. regional scale conductivity anomalies, *Phys. Earth planet. Int.,* **138,** 71–90, doi: 10.1016/S0031–9201(03)00078–5.

Schmucker, U., 1970. Anomalies of geomagnetic variations in the southwestern united states, in *Bull. Scripps Inst. Oceanogr.,* **13,** 1–165.

Smirnov, M.Y., 2003. Magnetotelluric data processing with a robust statistical procedure having a high breakdown point, *Geophys. J. Int.,* **152,** 1–7.

Sutarno, D. & Vozoff, K., 1991. Phase-smoothed robust m-estimation of magnetotelluric impedance functions, *Geophysics,* **56,** 1999–2007.

Szarka, L., 1988. Geophysical aspects of man-made electromagnetic noise in the earth—a review, *Surv. Geophys.,* **9,** 287–318.

Tikhonov, A. & Berdichevsky, M., 1966. Experience in the use of magnetotelluric methods to study the geological structures of sedimentary basins, *Izv. Acad. Sci. USSR Phys. Solid Earth,* **2,** 34–41 (English translation).

Travassos, J. & Beamish, D., 1988. Magnetotelluric data processing, *Geophys. J. R. astr. Soc.,* **93,** 377–391.

Tzanis, A. & Beamish, D., 1989. A high-resolution spectral study of audio-magnetotelluric data and noise interaction, *Geophys. J.,* **97,** 557–572.

Weckmann, U., Ritter, O. & Haak, V., 2003. A Magnetotelluric study of the Damara Belt in Namibia 2. internal structure of the Waterberg Fault/Omaruru Lineament, *Phys. Earth planet. Int.,* **138,** 91–112, doi: 10.1016/S0031–9201(03)00079–1.

Weidelt, P. & Kaikkonen, P., 1994. Local 1-D interpretation of magnetotelluric B-polarization impedances, *Geophys. J. Int.,* **117,** 733–748.